ORIGINAL RESEARCH

Inhibition of Ovarian Cancer Growth, Metastasis and Reverse the Tumor Microenvironment by Dual Drug-Loaded Polymer Micelle Targeting Tumor Microenvironment

Lu Zhang[1,2], Ruibo Guo[1,2], Muhan Chen[1,2], Mo Liu[1,2], Yang Liu[1,2], Yang Yu[1–3], Juan Zang[1,2], Liang Kong[1,2,*], Xuetao Li[1,2,*]

[1]School of Pharmacy, Liaoning University of Traditional Chinese Medicine, Dalian, People's Republic of China; [2]Shenyang Key Laboratory of Targeted Delivery of Chinese Medicine, Liaoning University of Traditional Chinese Medicine, Shenyang, People's Republic of China; [3]Key Laboratory of Ministry of Education for TCM Viscera-State Theory and Applications, Liaoning University of Traditional Chinese Medicine, Shenyang, People's Republic of China

*These authors contributed equally to this work

Correspondence: Liang Kong; Xuetao Li, School of Pharmacy, Liaoning University of Traditional Chinese Medicine, Shenyang Key Laboratory of Targeted Delivery of Chinese Medicine, Shengming 1 Road 77, Double D Port, Dalian, 116600, People's Republic of China, Email liangkong_sy@163.com; lixuetao1979@163.com

Introduction: Ovarian cancer is a malignant tumor that arises in the female reproductive system and is associated with a very high mortality rate. This is primarily due to the highly invasive nature of metastasis and recurrence. Transforming the immune environment from an immunosuppressive state to an anti-tumor state through the phenotypic transformation of tumor-associated macrophages is crucial for inhibiting the growth, metastasis, and recurrence of ovarian cancer.

Methods: A polymer micelle (RC-PH-Ms) containing paclitaxel (PTX) and honokiol (HNK) was designed based on high expression of reactive oxygen species in the tumor microenvironment. Once the micelles are actively targeted to the tumor microenvironment characterized by elevated levels of reactive oxygen species, the responsive bond is cleaved, thereby exposing the secondary targeting ligand C7R. The released PTX and HNK facilitate the transformation of relevant macrophages in the tumor microenvironment from an M2 phenotype to an M1 phenotype, which in turn inhibits tumor growth, invasion and metastasis, inhibit angiogenesis and reduce tumor recurrence.

Results: The effects of RC-PH-Ms on modulating the immune microenvironment and inhibiting tumor growth, invasion and metastasis, vascularization and recurrence were investigated both in vivo and in vitro.

Conclusion: RC-PH-Ms can significantly inhibit the metastasis and recurrence of ovarian cancer, which provides a new perspective for clinical treatment.

Keywords: ovarian cancer, tumor metastasis, recrudescence, immunotherapy, polymer micelle

Introduction

Ovarian cancer is a malignant tumor that arises within the female reproductive system. Its incidence ranks second only to that of cervical and endometrial cancers; however, it has the highest mortality rate among these cancers. This cancer significantly jeopardizes women's health.[1,2] The primary factors contributing to the low survival rate among ovarian cancer patients are recurrence and metastasis.[3,4] Ovarian cancer is characterized by a pronounced ability to invade and metastasize, allowing tumor cells to disseminate to various organs and tissues in the body via hematogenous and lymphatic pathways.[5,6] Lungs are the most common sites of metastasis for ovarian cancer, attributable to their abundant blood supply and lymphatic vessels that facilitate the spread of cancer cells.[7] Standard treatment for ovarian cancer typically involves maximal cytoreduction to decrease tumor size, followed by chemotherapy. Although some patients

exhibit favorable responses to chemotherapy, its effectiveness is often limited, and it is associated with significant adverse effects, leading to obviously relapse in a considerable proportion of patients. According to the International Federation of Gynecology and Obstetrics classification, over 70% of ovarian cancer cases diagnosed at stage III or I are known to recur within the first five years.[8] Consequently, the development of safe and effective treatment methods for ovarian cancer is critically necessary.

The response of treatment for ovarian cancer cell is regulated by numerous dynamic characteristics within the tumor microenvironment (TME).[9] The TME comprises tumor cells, immune cells, fibroblasts, vascular cells, and extracellular matrix, and is characterized by immunosuppressive properties, high expression of reactive oxygen species (ROS) and acidic conditions.[10,11] Within this environment, tumor-associated macrophages (TAMs) represent one of the most abundant immune cell types, playing an important role from onset to metastasis.[12–14] Various factors within the TME promote TAMs differentiation into the M2 phenotype, which secretes pro-angiogenic and immunosuppressive cytokines that facilitate tumor growth and metastasis. Conversely, M1 phenotype macrophages produce a greater quantity of pro-inflammatory cytokines and enhance the phagocytosis of tumor cells.[15,16] The transition of TAMs from the M2 to M1 phenotype can induce dynamic changes in the tumor immune microenvironment, shifting it from an immunosuppressive state to an anti-tumor state, thereby inhibiting tumor growth and metastasis.[17–19]

Paclitaxel (PTX) is a natural secondary metabolite that is isolated and purified from the bark of the gymnosperm yew. It exhibits significant anti-tumor effects and is recognized as one of the most effective anti-cancer drugs.[20] PTX can prevent microtubule depolymerization, thus inhibiting the mitosis of tumor cells and eventually leading to tumor cell death. Additionally, PTX has the capacity to activate macrophages, promote their secretion of pro-inflammatory cytokines, enhance their phagocytic ability, and stimulate anti-tumor immunity.[21,22] However, PTX is associated with several disadvantages including peripheral neuropathy, neutropenia, heart rate disorders, and other side effects. Its poor solubility also poses challenges for its clinical use. Traditional formulations for paclitaxel injection employ polyox-yethylated castor oil and absolute ethanol as solvents. Unfortunately, this approach often results in allergic reactions and may exacerbate peripheral neuropathy.[23,24] Therefore, it is urgent to develop safe and effective drug carriers.

Traditional Chinese medicine and its derivatives are characterized by low toxicity and high efficacy which have garnered significant clinical interest and are gradually emerging as potential cancer treatment agents.[25,26] Honokiol (HNK), a lignan compound isolated from the traditional Chinese medicinal herb Magnolia officinalis, exhibits multi-target effects including the inhibition of tumor growth, induction of tumor cell apoptosis and suppression of tumor vascularization.[27] Furthermore, HNK can reduce M2 macrophage markers and inhibit lung metastasis of tumors.[28] It is important to note that the low water solubility of HNK adversely affects its bioavailability, limiting its applicability in pharmaceutical formulations and clinical settings. To address the issue of low water solubility, we introduced a carrier for drug delivery. Due to the small particle size, internal hydrophobicity, protective effects of external chain segments, solubilization capabilities and low toxicity, polymer micelles have emerged as a significant option in contemporary drug delivery systems.[29] Modifying targeting ligands on the surface of polymer micelles can significantly enhance active targeting. The cell-penetrating peptide A7R (ATWLPPR) demonstrates high affinity and specificity for the overexpressed VEGFR-2 receptor present in various tumors.[30] A novel A7R-based tumor blood vessel and tumor cell-targeting penetrating peptide, Cyclo-A7R-RRR (C7R), has been designed and synthesized, which can enhance tumor cell membrane permeability and maintain stability of A7R.[31]

In this study, a polymer micelle containing PTX and HNK was designed and prepared based on high expression of ROS in the tumor microenvironment. In the micelles, $TPGS_{1000}$ and Soluplus were used as membrane materials, effectively encapsulating the insoluble PTX and HNK. The micellar surface was modified with $DSPE-PEG_{2000}$-C7R and $DSPE-PEG_{2000}$-thioketal (TK)-PEG_{5000}, respectively. The TK bond can undergo chemical bond cleavage in the presence of ROS, resulting in the formation of a ketone and a thiol. After micelles were actively targeted to the TME characterized by high ROS expression via systemic circulation, the TK bond in $DSPE-PEG_{2000}$-TK-PEG_{5000} was cleaved, revealing the secondary targeting ligand $DSPE-PEG_{2000}$-C7R, which facilitates the delivery of PTX and HNK to tumor cells via the usage of penetrating peptide. This process regulated the transformation of relevant macrophages in the tumor microenvironment from the M2 phenotype to the M1 phenotype, thereby inhibiting tumor growth, invasion, and metastasis, as well as angiogenesis and tumor recurrence. This low-toxicity localized treatment presents a novel

approach to addressing tumor metastasis and recurrence. The anti-tumor strategy diagram of RC-PH-Ms is shown in the supplementary material Scheme S1.

Materials and Methods

Materials

P-glycoprotein inhibitor D-alpha-Vitamin E polyethylene glycol succinate (TPGS$_{1000}$), Paclitaxel, Honokiol, 3,3,3,3-tetramethylindotricarbocyanineiodide (DiR), EdU-488 cell proliferation assay kit, one-step TUNEL apoptosis assay kit and HE staining kit were purchased from Meilun Co., Ltd. (Dalian, China). Polyethylene glycol-distearoyl phosphatidylethanolamine (DSPE-PEG$_{2000}$) was purchased from NOF Co., Ltd. (Tokyo, Japan). KRRRLPER, DSPE-PEG$_{2000}$-NHS and DSPE-PEG$_{2000}$-TK-PEG$_{5000}$ were synthesized and provided by Xian Ruixi Biological Technology Co., Ltd. (Xian, China). Soluplus was purchased from BASF New Materials Co., Ltd. (Shanghai, China). Live and dead cell staining kits and apoptosis-Hoechst staining kits were provided by EallBio Life Sciences, Inc. (Beijing, China). Ki-67 and VEGF antibodies were purchased from Boster Co., Ltd. (Wuhan, China). CD86, CD206, CD4, CD8 and F4/80 antibodies were supplied by Abcam (Cambridge, MA, USA). Other chemicals were of analytical or chromatographic grade.

Mouse ovarian epithelial cancer cells (ID8) were obtained from the Institute of Basic Medical Science, Chinese Academy of Medical Science (Beijing, China). The complete medium for ID8 cells included DMEM, 10% fetal bovine serum (FBS) and 1% penicillin–streptomycin solution (100 U/mL penicillin and 100 μg/mL streptomycin). The cells were cultured at 37 °C of 5% CO_2. All of the complete mediums were obtained from GIBCO (Billings, MT). C57BL/6 mice (18 ~ 22 g) were obtained from Liaoning Changsheng Biological Co., Ltd. (Shenyang, China). This study was approved by the Ethics Committee of Liaoning University of Traditional Chinese Medicine in accordance with the institution's animal care and use guidelines. The experimental animals were cultured in the experimental center with free drinking water and food and natural light at 20–25°C.

Synthesis of DSPE-PEG$_{2000}$-C7R

The synthetic route was shown in Figure S1. One hundred milligrams of DSPE-PEG$_{2000}$-NHS were dissolved in 3 mL DMF. The peptides KRRRLPER (1.1 eq) and triethylamine (3 eq)were added, reacted at room temperature for 12 h, and the reaction solution was transferred to a dialysis bag containing 2000 Da. After dialysis in pure water for 24 h, the product was collected by freezing and drying. The synthesis of DSPE-PEG$_{2000}$-C7R was detected by ^{1}H-nuclear magnetic resonance.[1H-NMR]

Construction of Nano Drug Delivery System

ROS response targeting PTX and HNK micelles (RC-PH-Ms) were prepared by thin-film dispersion method.[32] Simply put, Soluplus, TPGS$_{1000}$, DSPE-PEG$_{2000}$, DSPE-PEG$_{2000}$-C7R, DSPE-PEG$_{2000}$-TK-PEG$_{5000}$, PTX and HNK were dissolved in methanol at a molar ratio of 241:24:3:2:1:5:15 in a round bottom flask, and dried to a thin film using a rotary evaporator at 37°C. The film was hydrated with 5 mL PBS at 40°C and penetrated three times through a 0.22 μm polycarbonate membrane to obtain RC-PH-Ms. A series of micellar formulations were shown in Table S1. Blank micelles (Blank-Ms), paclitaxel micelles (PTX-Ms), honokiol micelles (HNK-Ms), paclitaxel and honokiol micelles (PH-Ms), and targeted micelles of paclitaxel and honokiol (C-PH-Ms) were prepared respectively. Coumarin (Cou) and DiR were used instead of drugs as fluorescent probes to prepare micelles in vitro and in vivo experiments.

Characterization of Nano Drug Delivery System

The morphology of micelles observed by transmission electron microscopy (TEM, Tecnai G220ST, FEICo., Tokyo, Japan). Drug inclusion in micelles was analyzed by Fourier transform infrared spectroscopy (FTIR). The critical micelle concentration (CMC) was determined using the pyrene fluorescent probe method. Add a backup solution of pyrene to the test tube and let it dry naturally overnight in the dark. The final concentration of pyrene was 2×10^{-6} M by adding Blank-Ms with different concentrations. After placing it overnight in a dark place, fluorescence spectra were recorded at 340 nm of absorbed light and 300–360 nm of excited light, respectively.

The particle size, polydispersity coefficient (PDI), and Zeta potential of micelles were measured using Nano Series Zen 4003 Zetasizer (Litesizer 500; Anton Paar Instruments Ltd., Graz, Austria). To determine the encapsulation efficiency (EE) of PTX and HNK, the concentrations were measured using a high-performance liquid chromatography system (HPLC, D1100, Dalian Elite). EE was calculated using the following formula: EE (%) = $(W_1/W_2) \times 100\%$, where W_1 represented the encapsulation mass of PTX and HNK after passing through a 0.22 μm polycarbonate film, and W_2 represented the total mass of PTX and HNK. To analyze the stability of the micelles, RC-PH-Ms were stored at 4 °C and room temperature (25 °C) for 15 d. EE was measured at 3, 6, 9, and 12 d, respectively. In addition, the microenvironmental responsiveness of RC-PH-Ms was also studied. To evaluate the intelligent response behavior, 0.1 mm H_2O_2 was added to RC-PH-Ms and incubated for 2 h, and the changes in particle size were detected.

Targeting Investigation in vitro

ID8 cells in logarithmic growth phase were inoculated into a 6-well plate at 4×10^5 cells/well. Coumarin micelles (Cou-Ms), targeted coumarin micelles (C-C-MS), ROS responsive-targeted micelles (RC-C-Ms), H_2O_2 and ROS responsive-targeted micelles (H_2O_2+RC-C-Ms, Cou final concentration of 3 μM) were added and incubated at 37 °C for 4 h and Blank-Ms were used as blank control. After washing three times with PBS, the cells were collected in 350 μL PBS and the fluorescence intensity of Cou was measured using a FACScan flow cytometer (BD Biosciences, NJ, USA). Similarly, ID8 cells in logarithmic growth phase were seeded into a 48-well plate at 1.5×10^4 cells/well. Blank-Ms, Cou-Ms, C-C-Ms, RC-C-Ms, H_2O_2+RC-C-Ms (Cou final concentration of 3 μM) were added into plate separately and incubate at 37 °C for 4 h. The cells were washed three times with PBS and fixed with paraformaldehyde (4%) at room temperature for 15 min. The nuclei were stained with Hoechst 33258 in the dark for 10 min and the uptake of cells was observed using a fluorescence microscope (Nikon Eclipse E800, Nikon, Tokyo).

Study on Synergistic Effect of Two Drugs

SynergyFinder was used to determine the synergistic effect of PTX and HNK. ID8 cells were inoculated into a 96 well plate at a density of 1.5×10^4 cells/well and then the inhibitory effects of PTX-Ms and HNK-Ms were analyzed at different concentrations (28, 14, 7, 3.5, 1.75, 0.875, 0.4375, 0 μM). After 48 h of treatment at 37°C, the cell viability was detected using the SRB method. The online SynergyFinder software was used to calculate collaborative scores based on survival index and zero interaction effectiveness.

Antitumor Effect in vitro

ID8 cells in logarithmic growth phase were inoculated into a 96 well plate at a density of 1.5×10^4 cells/well. PTX-MS, HNK-Ms, PH-Ms, C-PH-Ms and RC-PH-Ms were diluted in gradient and added them to the plate at 37 °C for 48 h. Blank-Ms were used as blank control. The culture medium was discarded and the SRB method was used to investigate the cytotoxicity of micelles. About 200 μL of 10% trichloroacetic acid was added to each well and fixed at 4 °C for 1 h. The plate was washed with distilled water three times and stained with 0.4% SRB for 20 min. The plate was washed with 1% acetic acid solution and 200 μL of 10 mm Tris alkaline solution were added to each well. The plate measured the absorbance at 540 nm. The cell survival rate was calculated using the following formula: Cell survival rate % = $(A_1/A_0) \times 100\%$, where A_1 represented the absorbance value at 540 nm of the cells after administration, and A_0 represented the absorbance value at 540 nm of the blank control group. The half maximal inhibitory concentration (IC_{50}) was calculated using GraphPad Prism software version 6.0. At the same time, a live/dead cell staining kit was used to stain in the dark for 30 min after inoculating the cells according to the above method and administering them for 24 h. Cells were observed by a fluorescence microscope.

Effect on Proliferation and Apoptosis

EdU cell proliferation assay was used to investigate the inhibitory effect of micelles on the proliferation of ID8. ID8 cells in logarithmic growth phase were seeded in a 48 well plate at 1×10^4 cells/well. Different micelle formulations were given separately with PTX final concentration of 3 μM, incubated at 37 °C for 12 h, stained with EdU staining kit, and used Blank-Ms as blank control. Cell proliferation was observed by a fluorescence microscope. The statistical calculation of

EdU positive cell rate was as follows: Positive cell rate (%) = $n_1/n \times 100\%$, where n_1 represented the number of positive cells and n represented total number of cells. The Annexin V-FITC/PI double staining method was used to determine cell apoptosis. ID8 cells in logarithmic growth phase were seeded into a 6-well plate at 2×10^4 cells/well. PTX-MS, HNK-Ms, PH-Ms, C-PH-Ms, RC-PH-Ms, H_2O_2+RC-PH-Ms were added into plate with PTX final concentration of 3 μM and Blank-Ms were used as blank control. After incubation at 37 °C for 24 h, the cells were collected and resuspended in a binding buffer. Cells were stained according to Annexin V-FITC/PI staining kit, and quadrant plots were drawn based on flow cytometry results.

Inhibition of Invasion and Metastasis

Wound healing experiments and Transwell experiments were used to investigate the invasion and metastasis of cells. ID8 cells were inoculated into a 6-well plate at a rate of 1×10^5 cells/well. Three parallel lines were drawn using a sterile pipette tip when the cells grow to 80%. Different formulations were added to the fresh medium with PTX final concentration of 3 μM and observed at 0, 12 and 24 h. The calculation formula for wound healing rate was as follows: wound healing rate% = (1- S_t/S_0) × 100%, where S_t represented the scratch area at 12 or 24 h and S_0 represented the scratch area at 0 h, respectively. 1.5×10^4 cells were added to the upper chamber of Transwells, and FBS containing culture medium were added to the lower chamber. Treat cells in the upper chamber with different micelle formulations at 37 °C for 24 h. Clean the cells in the upper chamber. After fixing the cells in the lower chamber with 4% paraformaldehyde for 15 min, they were stained with 0.5% crystal violet solution and observed.

Inhibitory Effect on Blood Vessels

The inhibitory effect of different micelle formulations on blood vessels was investigated using the chorioallantoic membrane (CAM) assay and vasculogenic mimicry (VM) experiment. Fertilized eggs were incubated at 37 °C and 70% humidity. On the 8th day, some eggshells were removed to expose CAM. PTX-Ms, HNK-Ms, PH-Ms, C-PH-Ms, RC-PH-Ms and H_2O_2+RC-PH-Ms were added with PTX final concentration of 3 μM and continued incubating for 48 h, and Blank-Ms was used as blank control. A digital camera was used to capture CAM and analyzed the number of blood vessels. Matrigel (50 μL/well) was added to the 96-well plate and incubated at 37°C for 30 min until solidification. ID8 cells of logarithmic growth stage were inoculated into 96-well plates without FBS in the medium with 1.5×10^4 cells/well and different micellar preparations with PTX final concentration of 3 μM at 37°C for 4 h. Blank-Ms were used as the blank control. The VM channel was observed and photographed using an inverted microscope.

Effects on Immune Microenvironment

Tumor cells and macrophages were co-cultured to investigate the effects of different micelles on macrophages. RAW 264.7 cells were inoculated in the lower chamber and ID8 cells in the upper chamber, and different micellar preparations with PTX final concentration of 3 μM were added to the upper chamber at 37°C for 24 h. The lower chamber cells were fixed with 4% paraformaldehyde for 30 min and permeated with 1% TritonX-100 for 30 min. One percent BSA solution was closed at room temperature for 1 h. CD86-APC and CD206-PE antibodies were added and incubated at 4°C overnight. Finally, Hoechst 33342 was stained at room temperature for 15 min. The cells were observed under an inverted fluorescence microscope and analyzed with image J software. Similarly, flow cytometry was used to quantify M1 and M2 type macrophages to analyze their proportions.

Construction of Tumor Bearing Mouse Model and Investigation of Targeting in vivo

A mouse axillary ectopic tumor model was constructed by subcutaneous injection. 1.0×10^7 cells were suspended in normal saline and the cell suspension was inoculated in the axilla of the right forelimb of C57BL/6 mice. Tumor growth was observed daily, and tumor volume was measured with vernier calipers. Follow-up was performed when the tumor volume reached about 100 mm³. Normal saline, free DiR, DiR micelle (DiR-Ms), targeted DiR micelle (C-DiR-Ms) and ROS response targeted micelle (RC-DiR-Ms) were injected into the tail vein of tumor-bearing mice, respectively, with DiR content of 3 μg/ mouse. After the mice were anesthetized with isoflurane, the fluorescence distribution in vivo was observed at 2, 4, 8, 12, 24, 48 and 72 h using the imaging system of animals.

Study on the Effect of Tumor Inhibition in vivo

Tumor-bearing mice were randomly divided into 6 groups and treated with normal saline, PTX-Ms, HNK-Ms, PH-Ms, C-PH-Ms and RC-PH-Ms by tail vein injection (PTX, 3 mg/kg), once every two days, for a total of 5 times. Weight and tumor volume were recorded after initial administration. The tumor volume was calculated as follows: V (mm^3) = a × b^2/2, where a was the length of the tumor and b was the width of the tumor. The survival curve of mice was drawn and the mice were killed the next day at the last dose. Tumor tissue, heart, liver, spleen, lungs, and kidneys were embedded in paraffin wax and cut into 3–5 μm sections. HE staining was used to observe the morphology of tumor cells. The proliferation and apoptosis of tumor cells were analyzed by Ki-67 and TUNEL staining. The expression of vascular growth factor (VEGF) in tumor tissues was analyzed by immunofluorescence. The growth of perivascular cells in tumor tissues was detected by immunofluorescence staining of α-SMA and CD31. The expression of CD86, CD206, CD4 and CD8 in tumor tissues were analyzed by immunofluorescence.

Effect of Inhibiting Lung Metastasis of Ovarian Cancer

A mouse model of lung metastasis of ovarian cancer was constructed by injecting 1.5×10^6 ID8 cells into the tail vein of mice. Two weeks after the tumor cells were injected into the tail vein, normal saline, PTX-MS, HNK-Ms, PH-MS, C-PH-Ms and RC-PH-Ms were injected into the tail vein once every two days for a total of 5 times. The survival curve of mice was drawn to investigate the effects of different formulations on the survival of mice. The mice were killed the day after the last administration and the lung tissues were photographed and embedded. HE staining was used to observe the lung. The proliferation and apoptosis of tumor cells were analyzed by Ki-67 and TUNEL staining. The expression of VEGF was observed by immunofluorescence staining.

Inhibitory Effect of Tumor Recurrence

The mice were anesthetized and underwent tumor resection surgery to remove about 90% of the tumor tissue when the tumor volume was about 400 mm^3. Different micelle preparations were injected into the tail vein once every three days for a total of five times. The tumor volume of the mice was measured before each administration, and the survival curve of the mice was plotted.

Safety Evaluation of Preparation

The safety of different preparations was investigated in healthy mice. The mice were treated according to the treatment protocol in "Study on the Effect of Tumor Inhibition in vivo". HE staining was used to observe the heart, liver, spleen, lung and kidney of mice to evaluate the safety of the preparation. The whole blood of mice was collected one week after the end of the tail vein treatment, and the hematological indexes such as WBC, LYM, MON, GRA and RBC were detected.

Statistical Analysis of Data

Experimental data were expressed as mean ± standard deviation (Mean ± SD). t test was used for the analysis between two groups, and ANOVA was used for the analysis between multiple groups. $p<0.05$ was considered statistically significant. * indicated $p<0.05$, ** indicated $p<0.01$, *** indicated $p<0.001$ and ****$P<0.0001$.

Results and Discussion

Characterization of Preparations

In this study, we prepared an RC-PH-Ms using a thin film dispersion method. This micelle incorporated the amphiphilic non-ionic polymer material Soluplus and the surfactant TPGS$_{1000}$ as membrane components. The poorly soluble drugs PTX and HNK were encapsulated within the core-shell structure of the micelle, while the ROS switch and active targeting ligands were modified on the micellar surface. We first synthesized and characterized the targeting ligands, with the ^{1}H-NMR spectrum of DSPE-PEG$_{2000}$-C7R presented in Figure S2. Following the successful synthesis of the targeting ligand, TEM was employed to observe the prepared micelle. Figure 1A illustrates that the surface of the RC-PH-Ms was
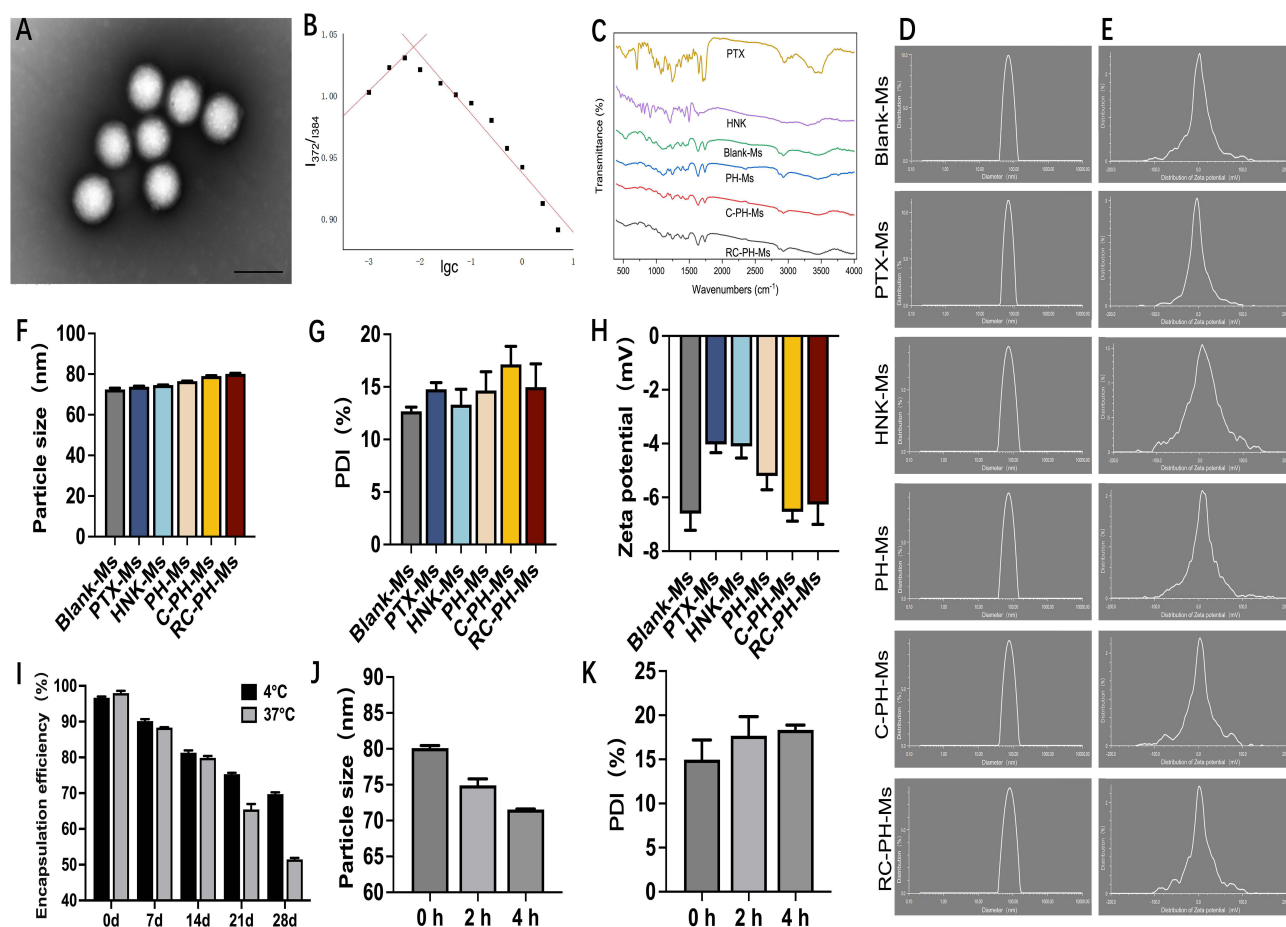
Figure 1 Characterization of micelles. (**A**) SEM image of RC-PH-Ms. Scale bar, 100 nm. (**B**) CMC determination for RC-PH-Ms. (**C**) IR spectra of various micelles. (**D**) Representative images of different micelles sizes. (**E**) Representative images depicting the Zeta potential of various micelles. (**F**) Particle size analysis of different micelles. (**G**) PDI values for the micelles. (**H**) Zeta potential measurements of different micelles. (**I**) Stability assessment results for RC-PH-Ms. (**J** and **K**) Investigation results regarding the responsiveness of RC-PH-Ms to ROS. Data were presented as mean ± SD (n = 6).

smooth, evenly dispersed, and spherical. The micelle was also spherical after TK bond cleaved, and its TEM image was shown in Figure S3.

To evaluate the micellization ability of RC-PH-Ms, we employed fluorescence spectroscopy of pyrene to determine the CMC.[33] As illustrated in Figure 1B, the relationship between the ratio of I_{372}/I_{384} and the logarithm of the RC-PH-Ms concentration (logC) was presented. At low concentrations of RC-PH-Ms, the drug existed predominantly in monomeric form within the solution. However, as the concentration of RC-PH-Ms exceeded the CMC, hydrophobic pyrene molecules began to solubilize within the internal hydrophobic regions of the micelles, resulting in a change in the I_{372}/I_{384} ratio. Consequently, the CMC value of RC-PH-Ms, as determined by fluorescence spectrometry, was found to be 7.41 µg/mL. A lower CMC value was advantageous as it enhances the stability and structural integrity of the micelles upon entering systemic circulation. Figure 1C presents the FTIR spectra of free PTX, free HNK, Blank-Ms, PH-Ms, C-PH-Ms, and RC-PH-Ms. The free PTX exhibited stretching vibrations of hydroxyl (O-H) and carbonyl (C=O) groups near 3400–3500 cm^{-1} and 1740 cm^{-1}, respectively. The stretching vibration of the carbon-oxygen single bond (C-O) in free HNK was observed in the range of 1000–1300 cm^{-1}. Additionally, the vibration of the aromatic ring was characterized by an absorption peak at 1450–1500 cm^{-1}. The absorption peaks for PH-Ms, C-PH-Ms and RC-PH-Ms closely resemble those of Blank-Ms, with no distinct absorption peak for the drug detected. This observation suggested that the drug was effectively encapsulated.

Representative images of the particle size and Zeta potential of micelles are shown in Figure 1D and E. The particle size, Zeta potential and PDI of the micelles are illustrated in Figure 1F–H. The particle size of Blank-Ms was measured at

(72.44 ± 0.66) nm, with a Zeta potential of – (6.6 ± 0.62) mV and a narrow PDI. Upon encapsulation of PTX and HNK in the micelles, the particle size increased to (76.51 ± 0.12) nm, the Zeta potential changed to – (5.2 ± 0.52) mV and the PDI was recorded at (14.63 ± 1.79) %. After modifying the surface of the drug-loaded micelles with a ROS switch and a targeting ligand, the particle size further increased to (80.1 ± 0.36) nm, the Zeta potential was – (6.2 ± 0.74) mV and the PDI remained unchanged. RC-PH-Ms exhibited a smaller particle size, which enhanced the effective utilization of the enhanced permeability and retention (EPR) effect, allowing for deeper penetration into tumor tissue. This characteristic contributed to a higher accumulation rate and an extended systemic circulation time at the tumor site. The electronegative nature of the micelles allowed them to interact with positively charged cell membranes, thereby contributing to effective drug delivery.[34] The EE of RC-PH-Ms was (96.69 ± 0.32) %, indicating a robust encapsulation capability for PTX and HNK. To examine the storage stability of the micelles, we measured the changes in EE over a period of 28 d. The results, as shown in Figure 1I, indicated that the EE of the drug gradually decreased during this time, which may be attributed to some flocculation during storage. On the 20th day, the EE of RC-PH-Ms at 37°C and 4°C were (51.47±0.42) % and (69.73±0.52) %, respectively. These findings suggested that RC-PH-Ms exhibit an excellent sustained-release effect and are capable of better encapsulating active substances during long-term storage. To verify the responsiveness of RC-PH-Ms to ROS, we examined the particle size and PDI of RC-PH-Ms following treatment with H_2O_2. The results, illustrated in Figure 1J–K, indicated that the particle size decreased slightly within 4 h of treatment, suggesting that the micelles underwent shrinkage. However, the change in PDI was not significant, implying that the micelles exhibit enhanced stability in response to ROS and possess preferable long-term circulation capabilities.

Targeting Investigation in vitro

The results of the investigation into the ability of ID8 cells to uptake micelles and the targeting of these micelles are presented in Figure 2. Since both PTX and HNK lack fluorescence, the micelles were labeled with the green fluorescent dye Cou.[35] The phagocytosis of the micelles by ID8 cells was then observed using a fluorescence microscope (Figure 2A), with cell nuclei stained using Hochest33342. The blank control group exhibited no fluorescence due to the absence of Cou. The Cou-Ms group displayed the weakest fluorescence, while the RC-C-Ms group exhibited a moderate intensity of fluorescence. In contrast, the C-C-Ms and H_2O_2+RC-C-Ms groups demonstrated strong fluorescence with comparable intensity. Figure 2B corroborates these findings through quantitative analysis of fluorescence intensity using Image J. To achieve a more precise quantitative assessment of micellar uptake by ID8 cells, flow cytometry was employed with results illustrated in Figure 2C and 2D. The blank control group showed no fluorescence, and the fluorescence intensity across the experimental groups was ranked as follows: H_2O_2+RC-C-Ms > C-C-Ms > RC-C-Ms > Cou-Ms. This ranking aligned with the observations made through fluorescence microscopy. The modification of the cell-penetrating peptide DSPE-PEG$_{2000}$-C7R significantly enhanced the uptake of Cou-Ms by ID8 cells. However, after modification with DSPE-PEG$_{2000}$-TK-PEG$_{5000}$, the cellular uptake ability was found to be weaker compared to the unmodified version. This reduction in uptake may be attributed to the fact that DSPE-PEG$_{2000}$-TK-PEG$_{5000}$ encapsulates C-C-Ms within a hydration layer which diminishes the targeting efficacy of C7R. Upon the cleavage of the TK bond in response to H_2O_2, the exposure of the cell-penetrating peptide was expected to improve the targeting efficacy of the micelle.

Confirmation of Synergies

The synergy of PTX and HNK was assessed using SynergyFinder (Figure 3A–C), an interactive web application designed for the analysis and visualization of multidrug and multidose combination response data. In evaluating the potential synergy of a drug combination, SynergyFinder compares the observed combination response to the expected response, which was calculated using a synergy scoring model.[36,37] This comparison allowed for the classification of the drug combination as either synergistic or antagonistic, based on the deviation between the observed and expected responses. In SynergyFinder, synergy scores (δ-scores) and surface maps are generated from various synergy models, including HSA, Loewe, Bliss, and ZIP models. Specifically, δ-scores greater than 10, less than −10 and between −10 and 10 indicated synergistic, antagonistic and additive effects, respectively.[38,39] The analysis conducted using SynergyFinder revealed that PTX and HNK have a δ-score of 11.9, suggesting a synergistic effect.
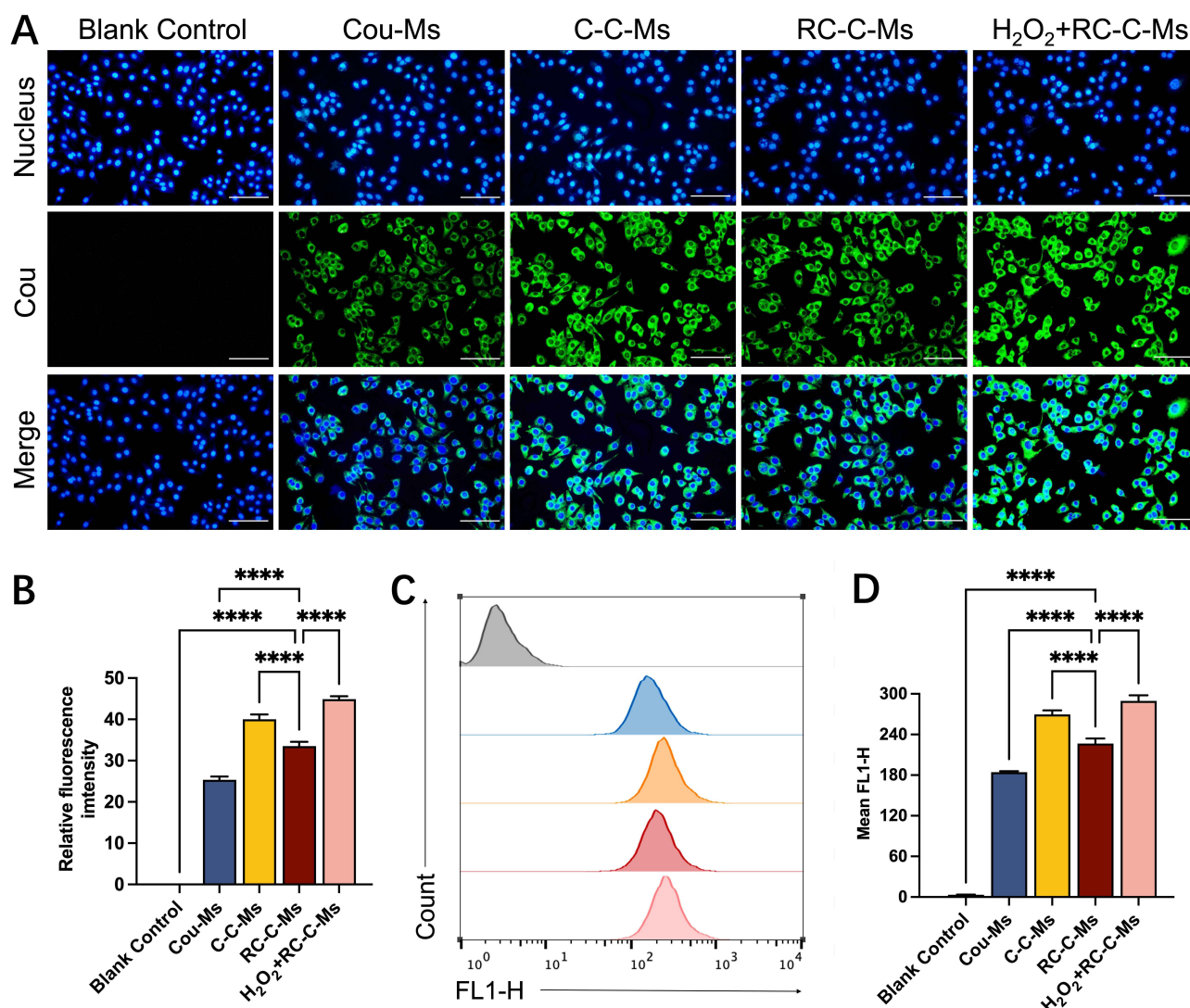
Figure 2 In vitro uptake of micelles and evaluation of targeting. (**A**) The uptake of different micelles by ID8 cells observed under a fluorescence microscope. Scale bar, 50 μm. (**B**) Quantitative analysis of fluorescence intensity. (**C**) The cellular uptake of micelles measured by flow cytometry. (**D**) The average fluorescence intensity of the cells. Data were presented as mean ± SD (n = 6). ****$P<0.0001$.

Cytotoxicity in vitro

The SRB method was employed to assess the toxicity of various micelles on ID8 cells, with the results presented in Figure 3D. At the 48 h, the cell survival rates for the PTX-Ms, HNK-Ms, PH-Ms and RC-PH-Ms groups at a concentration of 28 μM were (32.47±1.11) %, (64.01±1.98) %, (17.73±4.83) % and (15.85±4.47) %, respectively. The C-PH-Ms group exhibited the lowest cell survival rate at only 14.07±3.39%. As the concentration of micelles increased, a more pronounced decline in ID8 cell viability was observed. The IC_{50} values for PH-Ms, C-PH-Ms and RC-PH-Ms were determined to be (2.93±0.72) μM, (1.45±0.29) μM and (2.75±0.27) μM, respectively (Figure 3E). Notably, when PTX and HNK were co-encapsulated in micelles, a stronger inhibitory effect on ID8 cells was observed compared to their individual use, thereby confirming the synergistic effect of PTX and HNK. Following modification with DSPE-PEG$_{2000}$-C7R, cell viability further decreased, attributed to the efficient drug delivery facilitated by cell-penetrating peptides. However, at the same concentration, the cell survival rate of the RC-PH-Ms group was lower than that of the C-PH-Ms group. This discrepancy may arise from the presence of the ROS response switch on the micelle surface, which could hinder the timely recognition of tumor cells by the targeting ligand, thereby impairing its ability to inhibit cell viability.
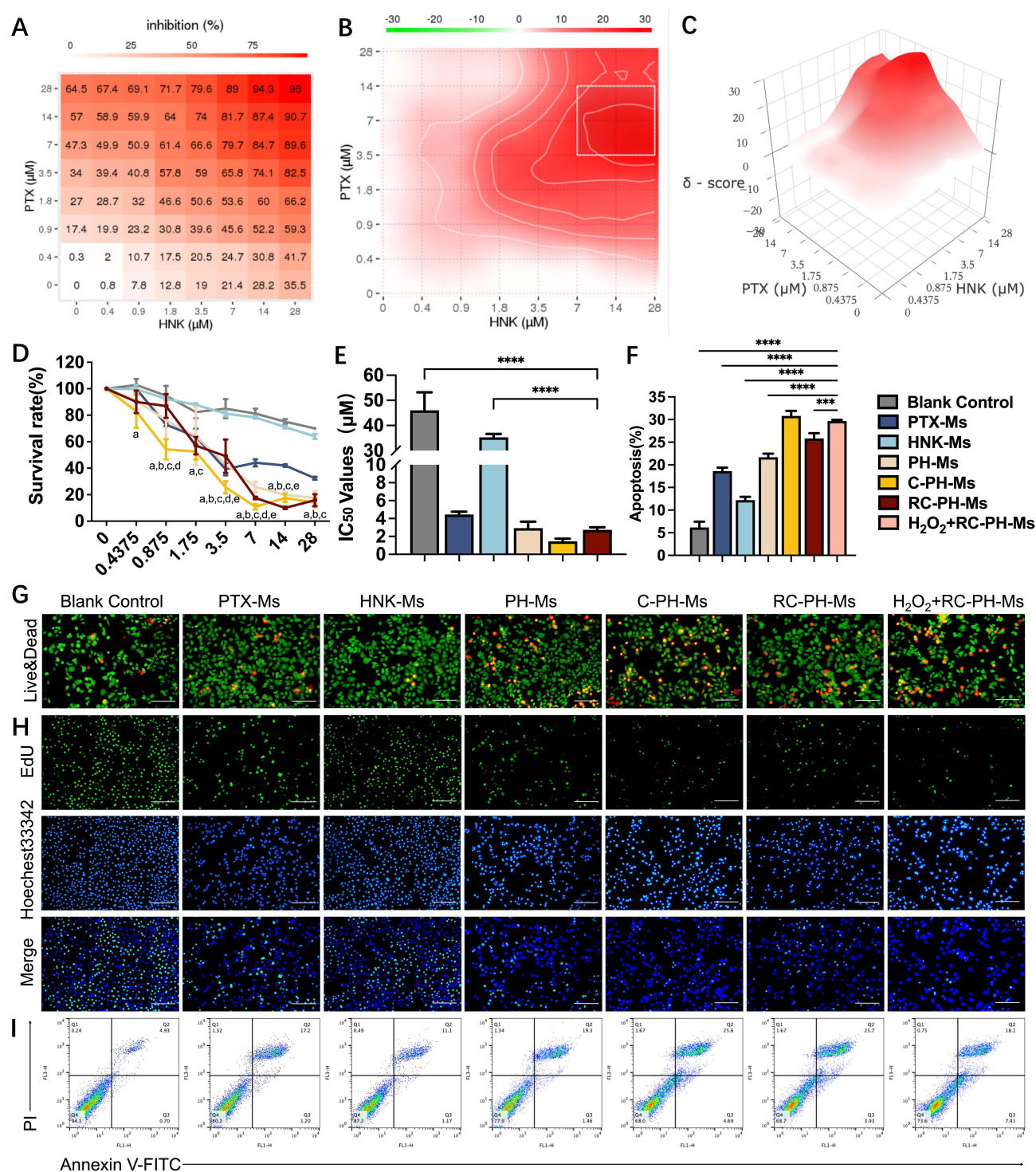
Figure 3 The cytotoxicity of various micellar formulations. (**A**) The dose–survival curves comparing PTX to HNK. (**B**) The heat map illustrated the responses to drug combinations. (**C**) 3D image corresponding to B. (**D**) The cytotoxicity of different micellar formulations against ID8 cells after 48 h. a, vs blank control; b, vs PTX-Ms; c, vs HNK-Ms; d, vs PH-Ms; e, vs C-PH-Ms. (**E**) The IC_{50} values of the micelles. (**F**) The apoptosis rates as measured by flow cytometry. (**G**) The representative images of live and dead cell staining. Scale bar, 50 μm. (**H**) The representative images from EdU proliferation experiments. Scale bar, 50 μm. (**I**) Apoptosis measurements obtained via flow cytometry. Data were presented as mean ± SD (n = 6). ***$P<0.001$, ****$P<0.0001$.

To enhance the visualization of the cytotoxic effects of RC-PH-Ms on tumor cells, calcein (green) and propidium iodide (red) were employed to stain living and dead cells subjected to different treatments. As illustrated in Figures 3G and S4, living cells appeared as green fluorescent dots, while dead or late apoptotic cells were represented as red

fluorescent dots. Notably, with the gradual administration of RC-PH-Ms, the number of red fluorescent spots increased, with the C-PH-Ms group exhibiting the highest count of dead cells. Although the RC-PH-Ms group displayed fewer dead cells compared to the C-PH-Ms group, following incubation with H_2O_2, the number of dead cells in the RC-PH-Ms group became comparable to that in the C-PH-Ms group. The results from the live and dead cell staining mirrored those of the cytotoxicity assays. The cytotoxicity trends observed for the various micelles against ID8 were largely consistent with the trends in cellular uptake. This indicates a strong correlation between cellular uptake and the enhanced in vitro anti-tumor efficacy of RC-PH-Ms.

Effect on Proliferation and Apoptosis

The EdU fluorescence experiment and flow cytometry were employed to assess the proliferation and apoptosis of ID8 cells, respectively. In Figure 3H, red fluorescence indicated EdU-positive cells, which were actively proliferating, while blue fluorescence represented all Hoechst-stained cells. The proliferation capacity of the cells was quantified by the ratio of EdU-positive cells to the total number of cells and the statistical results were shown in Figure S5. Results from the EdU fluorescence experiment revealed that, compared to the single-drug micelle group, micelles co-encapsulated with two drugs exhibited a reduced rate of EdU-positive cells. Specifically, the EdU-positive cell rates for the C-PH-Ms group and the H_2O_2+RC-PH-Ms group were (31.7±6.01) % and (28.93±7.09) %, respectively, both of which were lower than the rates of (40.06±6.35) % for the RC-PH-Ms group and (41.63±8.36) % for the PH-Ms group.

The FITC/PI kit was utilized to visually assess apoptosis. A strong FITC fluorescence signal was indicative of apoptotic cells, which can be categorized into early and late apoptosis based on the intensity of the PI signal.[40,41] The results are presented in Figure 3I and F. The cell apoptosis rates in the PTX-Ms group and HNK-Ms group were (18.61±0.77) % and (12.22±0.73) %, respectively. In contrast, the cell apoptosis rate in the PH-Ms group was (21.68±0.8) %. Following target modification, the cell apoptosis rate in the C-PH-Ms group increased to (30.83±1.11) %. The cell apoptosis rate in the RC-PH-Ms group was lower than that in the C-PH-Ms group; however, it increased after incubation with H_2O_2. Experimental results on proliferation and apoptosis indicated that, compared to micelles containing drugs alone, the co-encapsulation of PTX and HNK in micelles enhanced the inhibition of cell proliferation and promoted apoptosis. Although the inhibitory effect of RC-PH-Ms on tumor cells was weaker than that of C-PH-Ms, after incubation with H_2O_2, the inhibitory effect on tumor cell growth became comparable to that of C-PH-Ms. These findings aligned with the results from cellular uptake and cytotoxicity experiments, confirming the environmental responsiveness of RC-PH-Ms, the active targeting capability of targeting ligands and the synergistic effects of the drugs.

Inhibition of Invasion and Metastasis

The metastasis and invasion of surrounding tissues by tumor cells were critical pathological factors contributing to mortality from malignant tumors.[42,43] In this study, the scratch test was employed to evaluate the impact of micelles on the migration of ID8 cells. This assay allowed for a visual assessment of changes in cell migration within the scratch area. As illustrated in Figure 4A, B and D, the scratch area in the Blank Control group decreased significantly over 12 h, indicating pronounced cell migration. Conversely, the C-PH-Ms group and the H_2O_2+RC-PH-Ms group exhibited the largest scratch areas. After 24 h, the scratches in the Blank Control group were nearly healed. Both PTX-Ms and HNK-Ms demonstrated inhibitory effects on scratch healing; however, these effects were not particularly pronounced. In contrast, the PH-Ms and RC-PH-Ms groups displayed a more substantial inhibitory effect on cell migration. Notably, the C-PH-Ms group and the H_2O_2+RC-PH-Ms group consistently exhibited the strongest effects on cell migration, with wound healing rates of (9.34±4.03) % and (6.74±3.29) %, respectively.

To further validate the results of the migration experiment, we conducted Transwell assays to examine the impact of micelles on ID8 cell invasion. As illustrated in Figure 4C and E, the number of ID8 cells that traversed the polycarbonate membrane from the upper chamber of the Transwell chambers in the H_2O_2+RC-PH-Ms group was significantly lower compared to both the blank control and the single-drug micelles. The cell invasion rates for PTX-Ms, HNK-Ms, PH-Ms, C-PH-Ms, RC-PH-Ms, and H_2O_2+RC-PH-Ms were recorded as (70.85±5.13) %, (78.96±3.92) %, (48.98±5.48) %, (8.99±1.66) %, (34.58±5.62) % and (10.13±2.38) %, respectively. The inhibitory effects of the various micelles on ID8 cell invasion and metastasis mirrored the trends observed in their capacity to inhibit proliferation and metastasis.
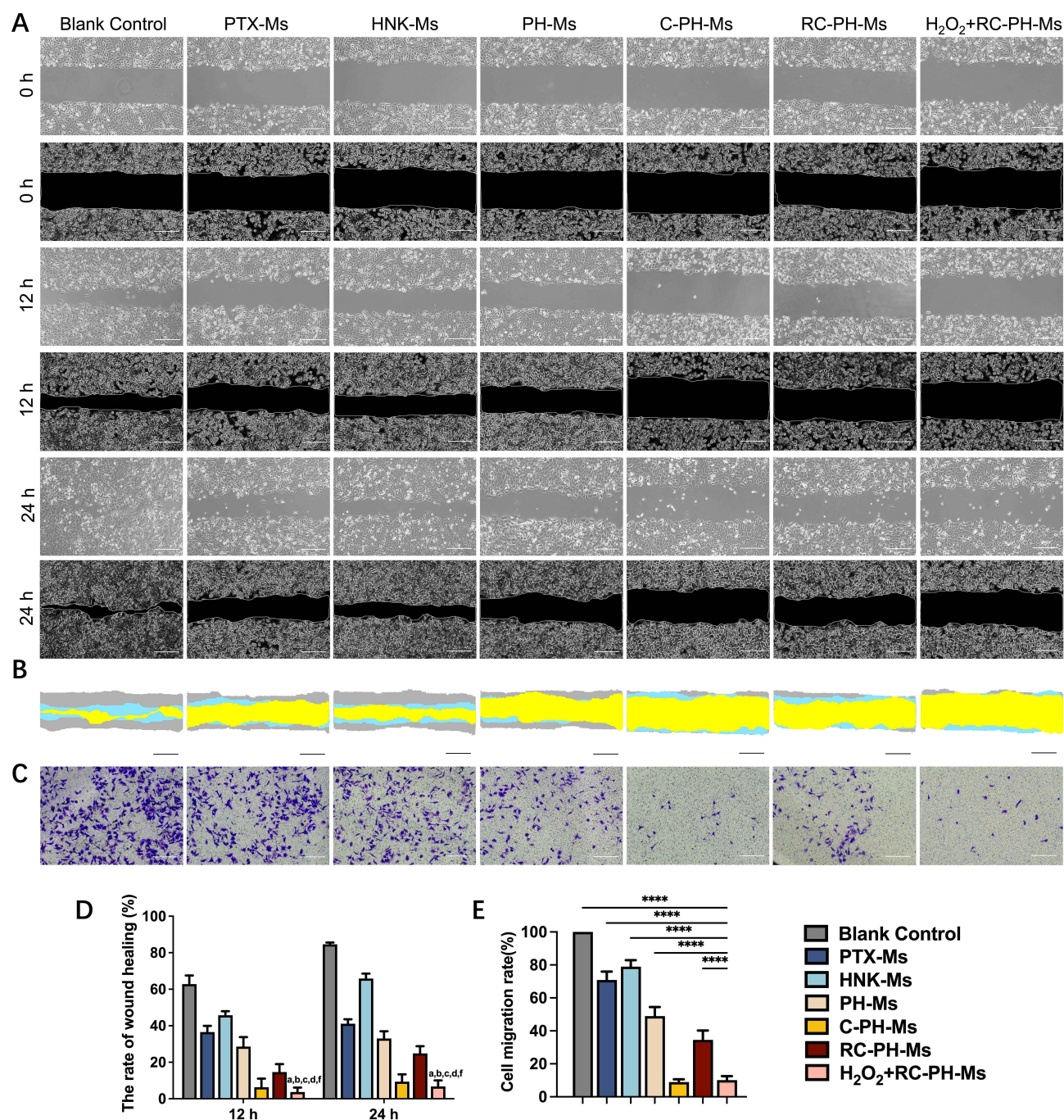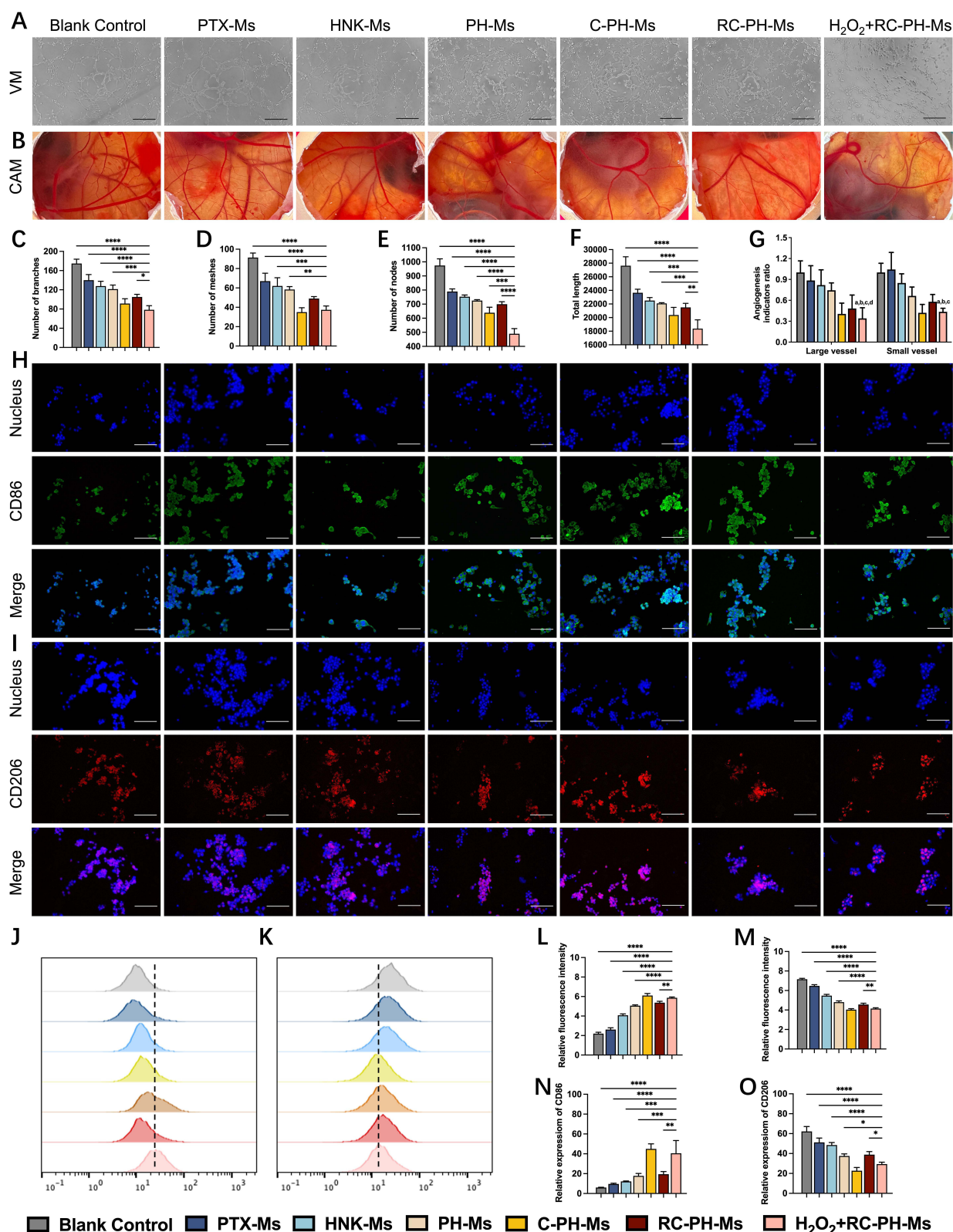
Figure 4 The effect of micelles on the invasion and metastasis of ID8 cells. (**A**) The scratch healing process at various time points following different micelle treatments. Scale bar, 50 μm. (**B**) Direct view of scratch healing. The gray area represented scratches at 0 h. The blue area represented scratches at 12 h. The yellow area represented scratches at 24 h. Scale bar, 50 μm. (**C**) ID8 cells passing through the Transwell chamber. Scale bar, 50 μm. (**D**) The rate of wound healing. a, vs blank control; b, vs PTX-Ms; c, vs HNK-Ms; d, vs PH-Ms; f, vs RC-PH-Ms. (**E**) The relative invasion rate of ID8. Data were presented as mean ± SD (n = 6). ****$P<0.0001$.

Inhibitory Effect on Blood Vessels

As tumors grow, the blood vessels within them become abnormal, leading to a hypoxic and acidic environment that promotes tumor invasion and metastasis.[44,45] VM refers to blood vessel-like structures found in blood vessel-dependent solid tumors. These structures are formed by highly invasive tumor cells through their own deformation and remodeling of the extracellular matrix, serving as a unique source of blood supply for the progression of aggressive tumors.[46,47] To investigate the effects of different micelles on the VM of ID8 cells, we observed the VM of cells through three-dimensional culture. As illustrated in Figure 5A, the number of tubular structures in both the C-PH-Ms group and the H$_2$O$_2$+RC-PH-Ms group decreased

Figure 5 The effects of various micelles on angiogenesis and immune cell infiltration. (**A**) Inhibition of VM after co-incubation with micelles. Scale bar, 50 μm. (**B**) Representative images from the CAM experiment. (**C-F**) The suppression rates of VM-related indicators. (**G**) The inhibition rates of micelles on large and small blood vessels in the CAM. a, vs blank control; b, vs PTX-Ms; c, vs HNK-Ms; d, vs PH-Ms. (**H** and **I**) The effects of micelles on the expression of CD86 and CD206 in RAW264.7 cells observed by fluorescence microscopy. Scale bar, 50 μm. (**J** and **K**) The impact of micelles on the expression of CD86 and CD206 in RAW264.7 cells detected by flow cytometry. (**L** and **M**) A quantitative analysis of fluorescence intensity. (**N** and **O**) The average fluorescence intensity of the cells. Data were presented as mean ± SD (n = 6). *$P<0.05$, **$P<0.01$, ***$P<0.001$, ****$P<0.0001$.

significantly. We conducted statistical analyses on the number of branches, meshes, nodes, and total length, with results presented in Figure 5C–F. Both the C-PH-Ms group and the H_2O_2+RC-PH-Ms group significantly inhibited the formation of VM. Building on this, we further verified whether the micelles could inhibit angiogenesis on the allantoic membrane of chicken embryos.[48,49]

As shown in Figure 5B and G, H_2O_2+RC-PH-Ms significantly inhibit the formation of both large and small blood vessels on the allantoic membrane of chicken embryos when compared to PTX-Ms and HNK-Ms. The incorporation of the membrane-penetrating peptide DSPE-PEG$_{2000}$-C7R markedly enhances the inhibitory effect of PH-Ms on angiogenesis, whereas the modification of the corresponding ROS switch diminishes the inhibitory effect of C-PH-Ms. Furthermore, H_2O_2+RC-PH-Ms exhibited a significant reduction in the formation of large blood vessels compared to PH-Ms. A series of studies have established that blood vessel formation was closely linked to tumor growth, invasion, metastasis, and prognosis. The growth, invasion, and metastasis of ovarian cancer are contingent upon angiogenesis, with the malignancy and prognosis of the disease being strongly associated with the density of blood vessels within the tumor.[50] Experimental results indicated that the RC-PH-Ms we developed had an inhibitory effect on both neovascularization and VM. This finding elucidated the effective inhibitory action of RC-PH-Ms on the invasion and metastasis of ID8 cells.

Effects on Immune Microenvironment

Under the influence of the local tumor microenvironment, TAMs are primarily polarized into two distinct types: classically activated M1-type TAMs and alternatively activated M2-type TAMs.[51] To simulate the tumor immune microenvironment in vitro, we incubated tumor cells with macrophages. Following the labeling of M1 and M2 macrophages with CD86 and CD206, respectively, we observed the morphology of the macrophages using a fluorescence microscope and the results are presented in Figures 5H and I, L and M. The results indicated that while the number of M1-type RAW 264.7 cells in the tumor microenvironment was initially low, treatment with different micelles resulted in an increase in the number of M1-type macrophages.

The expression levels of M1-type macrophages following various micelle treatments were ranked as follows: C-PH-Ms > H_2O_2 + RC-PH-Ms > RC-PH-Ms > PH-Ms > HNK-Ms > PTX-Ms > Blank control. Conversely, the expression of M2-type macrophages decreased with the lowest expression observed in the PH-Ms group. These results indicated that, macrophages in the immune microenvironment transitioned from the M2-type to the M1-type following different micelle treatments. In addition to fluorescence microscopy, we employed flow cytometry to quantify the expression of M1 and M2 macrophages (Figures 5J and K, N and O). The positive ratios of M1 and M2 types in the C-PH-Ms group were (44.97 ± 5.08) % and (22.67 ± 3.31) %, respectively, while the positive ratios in the H_2O_2 + RC-PH-Ms group were (40.5 ± 12.91) %and (29.37 ± 1.89) %, respectively. These findings demonstrated that C-PH-Ms and H_2O_2 + RC-PH-Ms exhibited the most pronounced capacity to convert macrophages from M2 to M1, corroborating the results obtained from fluorescence microscopy.

Tumor-associated macrophages play crucial roles in promoting cancer cell proliferation, angiogenesis, and immunosuppression within the tumor microenvironment, thereby facilitating tumor growth and metastasis. M1 macrophages are known to produce a range of anti-tumor factors, whereas M2 macrophages are associated with tumor growth, invasion, metastasis, and angiogenesis.[52,53] There was an increase in M1-type macrophages treated by RC-PH-Ms, which secreted substantial amounts of tumor-inhibiting growth factors, leading to the inhibition of tumor growth and proliferation. Conversely, M2-type macrophages decreased, indicating that tumor growth, invasion, metastasis, and angiogenesis were also inhibited.

Investigation of Targeting in vivo

Excluding the interference from auto-luminescence, mice in the blank control group did not exhibit fluorescence at any time point under identical imaging conditions. Free DiR in tumor-bearing mice was primarily metabolized by the liver, with a small fraction accumulating at the tumor site and being excreted 24 h post-administration. As illustrated in Figure 6, a distinctly observable fluorescence signal was detected in the tumor of mice 2 h after the injection of micelles by tail vein. The DiR-Ms, C-DiR-Ms, and RC-DiR-Ms groups reached their maximum fluorescence intensity at 4 h, after
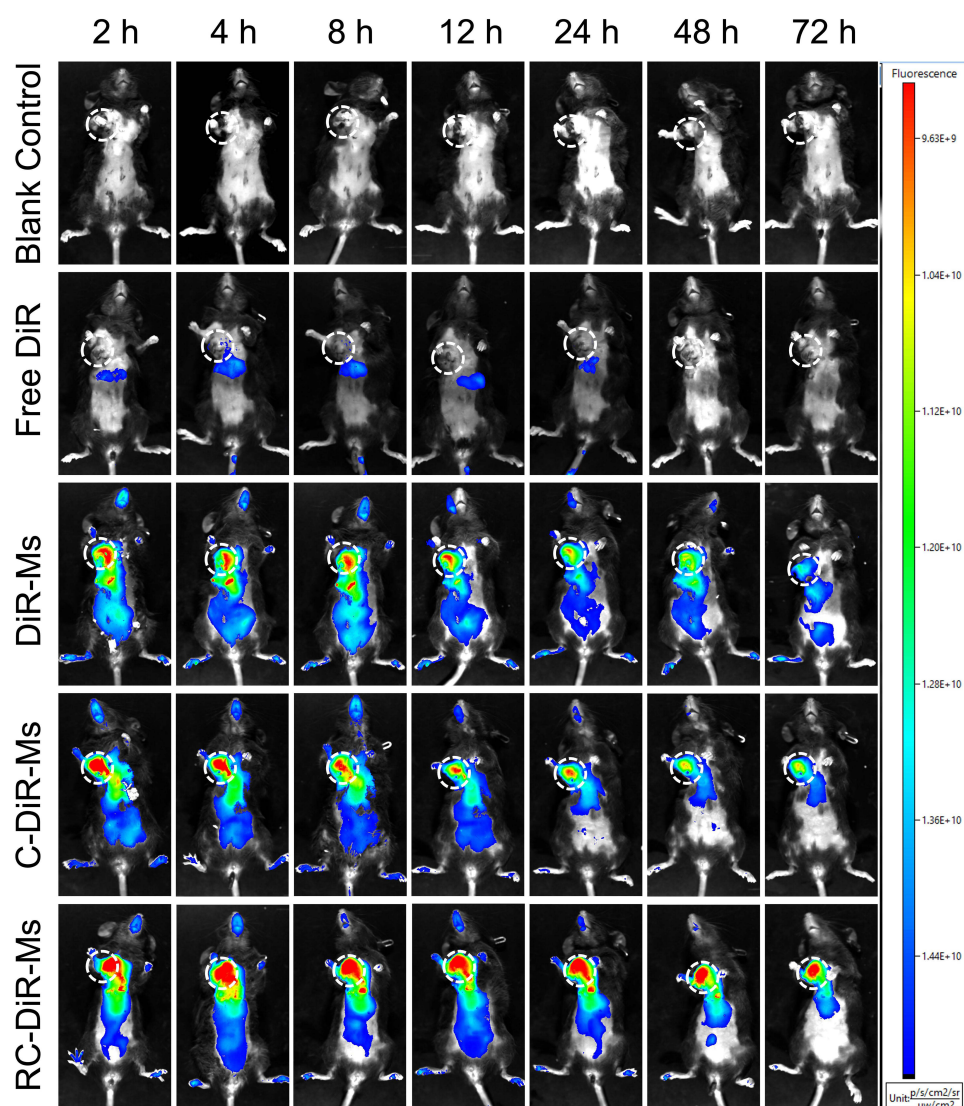
Figure 6 Representative images of real-time fluorescence imaging of tumor-bearing mice within 72 hours after tail vein injection of micelles. Circles indicating tumor sites.

which the intensity gradually decreased until 72 h. Under the same imaging conditions, the fluorescence intensity of the RC-DiR-Ms group was significantly higher at each time point compared to the DiR-Ms and C-DiR-Ms groups. This observation aligned with the cell imaging results in vitro suggested that drugs encapsulated in micelles modified with DSPE-PEG$_{2000}$-C7R and DSPE-PEG$_{2000}$-TK-PEG$_{5000}$ possessed favorable targeting properties.

Tumor Inhibition in Tumor-Bearing Mice

Following the demonstration of the ability to inhibit tumor cells in vitro, we proceeded to investigate the inhibitory effects of RC-PH-Ms on tumor-bearing mice. After administering various treatments and subsequently sacrificing the mice, the tumors were excised and representative images are presented in Figure 7A. The tumor growth curves and tumor inhibition rates are illustrated in Figure 7B and C. The tumor growth curves for the HNK-Ms group did not significantly differ from that of the blank control group, indicating that HNK-Ms were ineffective in delaying tumor growth. Conversely, the tumor growth in mice treated with other micelles was inhibited with the degree of inhibition ranked as follows: RC-PH-Ms > C-PH-Ms > PH-Ms > PTX-Ms > HNK-Ms > blank control. Figure 7D demonstrates that the weight loss experienced by tumor-bearing mice during treatment inversely correlates with the degree of tumor inhibition, thereby confirming the therapeutic efficacy of the micellar treatments. Statistical analyses of mouse survival revealed that
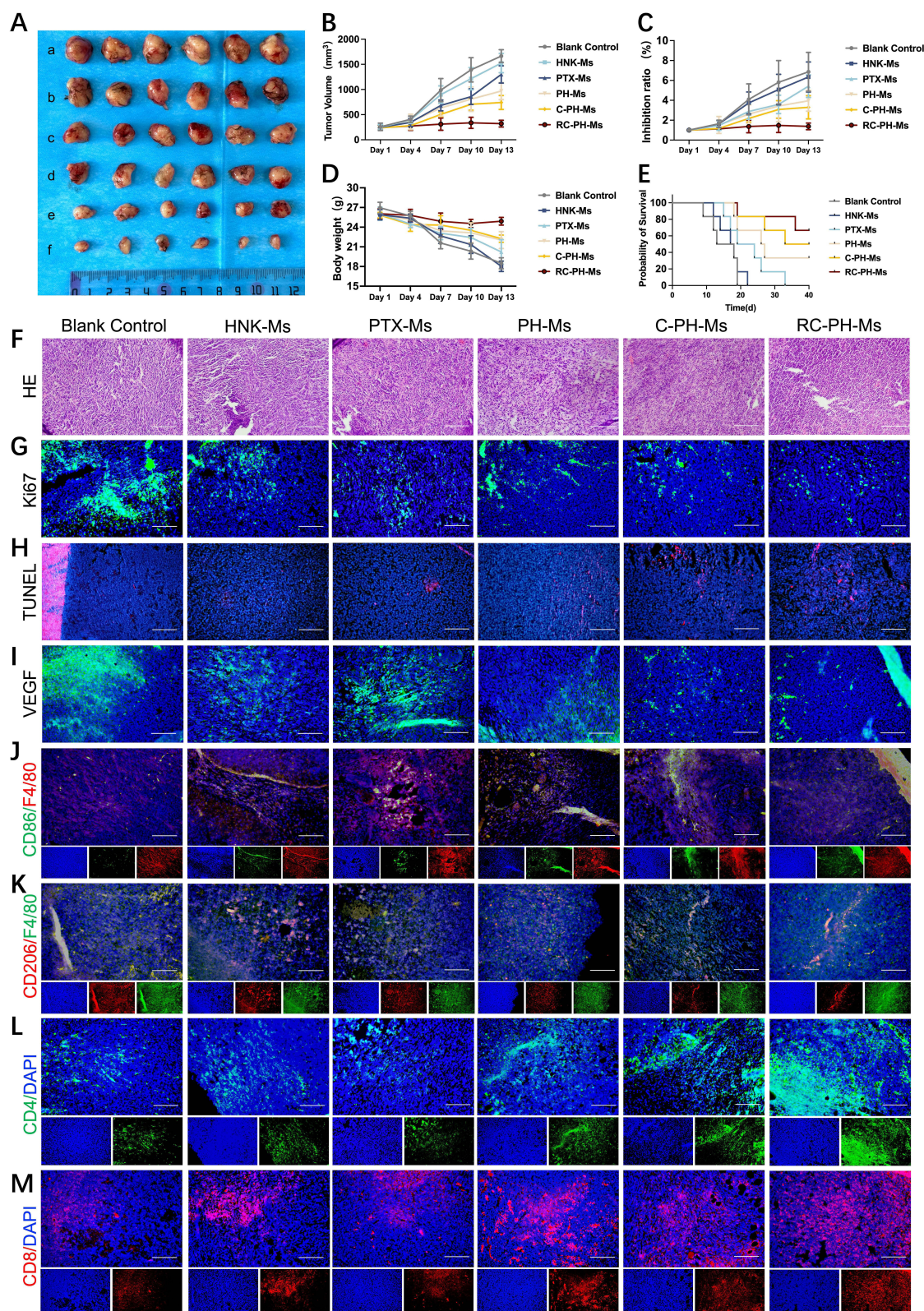
Figure 7 The therapeutic effects of micelles on ectopic tumor-bearing mice. (**A**) Representative images of tumors in treated mice. a, Blank control; b, HNK-Ms; c, PTX-Ms; d, PH-Ms; e, C-PH-Ms; f, RC-PH-Ms. (**B**) The changes in tumor volume across different groups of mice. (**C**) The tumor inhibition rates. (**D**) Body weight fluctuations of tumor-bearing mice during the treatment period. (**E**) The survival rate curve of the mice. (**F-H**), Representative images of HE staining (**F**), Ki-67 staining (**G**) and TUNEL (**H**) staining of tumors. (**I**) Representative images of VEGF expression. Scale bar, 50 μm. (**J-M**) The expression levels of CD86 (**J**), CD206 (**K**), CD4 (**L**), and CD8 (**M**) in tumor tissues. Scale bar, 50 μm. Data were presented as mean ± SD (n = 6).

all mice in the blank control, HNK-Ms, and PTX-Ms groups succumbed before completing the treatment cycle (Figure 7E). However, HNK-Ms and PTX-Ms generally extended the survival duration of the mice. Notably, the overall survival rates were improved in the PH-Ms, C-PH-Ms, and RC-PH-Ms groups, with the RC-PH-Ms group exhibiting the most pronounced effect.

HE staining was employed for the pathological analysis of tumor tissues (Figure 7F). In the blank control group, tumor cells exhibited active and dense growth, accompanied by a higher presence of atypical nuclei. Following various micelles treatments, the arrangement of tumor cells became irregular with a notable reduction in mitosis, necrosis, and atypical nuclei. The expression level of Ki67 protein was closely associated with tumor cell proliferation with the blank control group demonstrating the highest proliferation capacity. In contrast, micelle treatment significantly inhibited cell proliferation, particularly in the RC-PH-Ms group (Figures 7G, S6A). TUNEL staining was utilized to identify apoptotic cells within the tumor tissue. Interestingly, the results from TUNEL staining contradicted those of Ki67, revealing that the blank control group exhibited the lowest number of TUNEL-positive cells (Figure 7H). Conversely, the RC-PH-Ms group significantly enhanced cell apoptosis compared to the other groups (Figure S6B). These findings indicated that micelles effectively inhibited tumor cell proliferation and promoted apoptosis, thereby suppressing tumor growth. Additionally, immunofluorescence staining was conducted to assess the expression of VEGF in tumor tissues (Figures 7I and S6C). Following micelle treatment, VEGF expression in tumor tissues was found to decrease, with a significant reduction observed in the RC-PH-Ms group. These results suggested that micellar treatment can effectively inhibit angiogenesis within tumor tissues. Given that tumor invasion and metastasis were closely linked to angiogenesis, the observed inhibition of cell proliferation and angiogenesis, along with the promotion of apoptosis, collectively contributed to tumor suppression.

TAMs influence the immune microenvironment, regulating the type, intensity and duration of immune responses as well as tumor immune escape. During the tumorigenesis stage, TAMs predominantly express M1 macrophage markers. However, as cancer progresses, there is a notable shift in the macrophage phenotype from M1 to M2, with increasing numbers of M2 macrophages. We employed multiple-immunofluorescence markers, including F4/80, CD86, CD206, CD4 and CD8 to assess the infiltration of immune cells in the tumor tissue of tumor-bearing mice (Figures 7J–M and S6D–G). The results indicated that post-treatment, there was an increase in the distribution of CD86-labeled M1 macrophages, while the distribution of CD206-labeled M2 macrophages decreased. Additionally, the infiltration of immune cells such as CD4 and CD8 was observed to increase in tumor tissues. Notably, these findings were corroborated by cell experiments. Thus far, we have demonstrated that RC-PH-Ms enhance the tumor microenvironment by reducing the infiltration of M2 macrophages, which promote tumor progression, while simultaneously increasing the infiltration of M1 macrophages and other immune cells with anti-tumor functions, including CD4 and CD8 cells. This shift enhanced the immune microenvironment, inhibited tumor invasion and metastasis, reduced angiogenesis and ultimately slowed tumor growth in mice.

Effect of Inhibiting Lung Metastasis of Ovarian Cancer

Following the determination of the inhibitory effect on tumors, we investigated the anti-tumor invasion and metastasis effects of RC-PH-Ms in mice with lung metastasis. Figure 8A presents representative images of the lungs from mice exhibiting tumor lung metastasis after treatment with various drugs. In comparison to normal lungs, distinct nodules were observed in the lungs of the blank control group. Although the PH-Ms group displayed a relatively reduced number of nodules on the lung surface, a significant number of nodules remained within the lungs. In contrast, after treatment with RC-PH-Ms, nearly all nodule metastases were eliminated, suggesting that the combination of drugs exhibited a superior anti-metastatic effect in vivo. The survival curve and weight changes of mice after treatment are shown in Figure 8B–D.

Pathological observations of the lungs were conducted and the results are presented in Figure 8E and F. The alveolar structure in normal mice was distinctly visible, characterized by thin and uniform alveolar walls, with no apparent signs of inflammatory cell infiltration, fibrosis or other pathological changes. In contrast, the lung tissue of mice in the blank control group exhibited significant damage, with larger areas of tumor metastasis, indicating that substantial lung metastasis had occurred. PH-Ms demonstrated a moderate ability to reduce the risk of metastasis, with this inhibitory effect being more pronounced in the RC-PH-Ms group. Following the establishment of the lung metastasis model, all
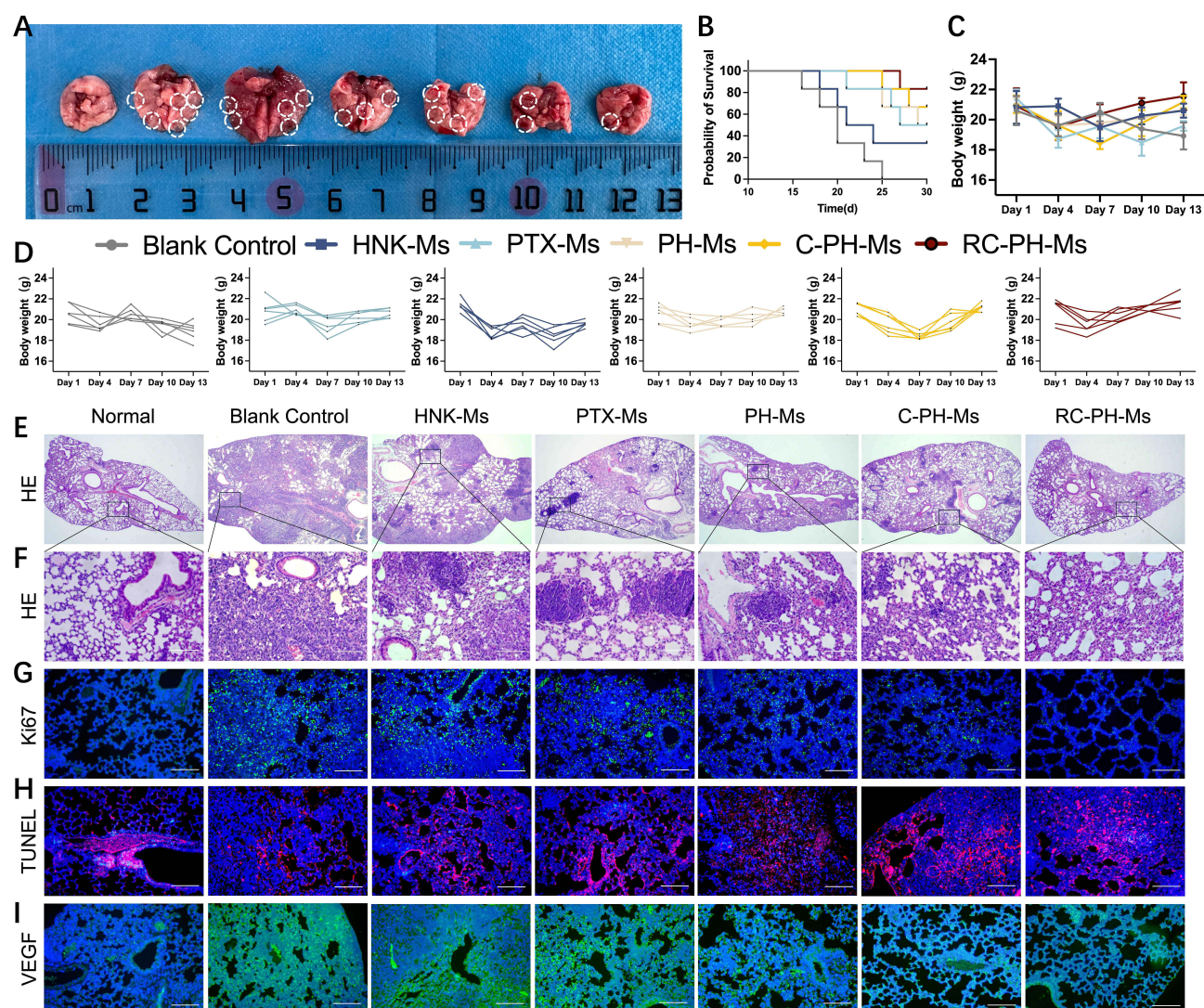
Figure 8 Effect of micelles on tumor lung metastasis. (**A**) Representative images of mouse lungs following micelle treatment. From left to right are healthy lungs, Blank control, HNK-Ms, PTX-Ms, PH-Ms, C-PH-Ms and RC-PH-Ms. Circles indicating nodule sites. (**B-D**) Survival rates (**B**) and body weight (**C** and **D**) curves of tumor-bearing mice during the treatment period. (**E** and **F**) HE staining of lung tissue at various magnifications under the microscope. Scale bar, 50 μm. (**G–I**). Representative images of immunofluorescence staining for Ki-67 (**G**), TUNEL (**H**) and VEGF (**I**) in lung tissue. Scale bar, 50 μm. Data were presented as mean ± SD (n = 6).

PBS-treated mice succumbed by day 25, while the RC-PH-Ms group exhibited the lowest mortality rate (Figure 8B). Ki67 and TUNEL staining results indicated that RC-PH-Ms effectively inhibited the proliferation of lung metastatic tumor cells and promoted their apoptosis (Figures 8G-H and S7A-B). Furthermore, the expression of VEGF in lung tissue was assessed, revealing that drug treatment suppressed VEGF expression (Figures 8I and S7C). This finding might elucidate the effective inhibition of tumor invasion and metastasis. The quantitative analysis results of the immuno-fluorescence staining were displayed in Figure S6.

Inhibitory Effect of Tumor Recurrence

In the context of tumor treatment, it was crucial to address the challenges posed by tumor recurrence.[54] After confirming that RC-PH-Ms effectively inhibited tumor growth, invasion and metastasis, we investigated their impact on tumor recurrence (Figure 9A). The tumor growth curves for mice in each group indicated that HNK-Ms, PTX-Ms and PH-Ms demonstrated limited efficacy in delaying tumor recurrence, whereas C-PH-Ms and RC-PH-Ms significantly delayed recurrence. On day 13, the average tumor volume of mice in the RC-PH-Ms group was measured at (309.43 ±99.16) mm,[3] representing only 27.18% of the average tumor volume observed in the blank control group
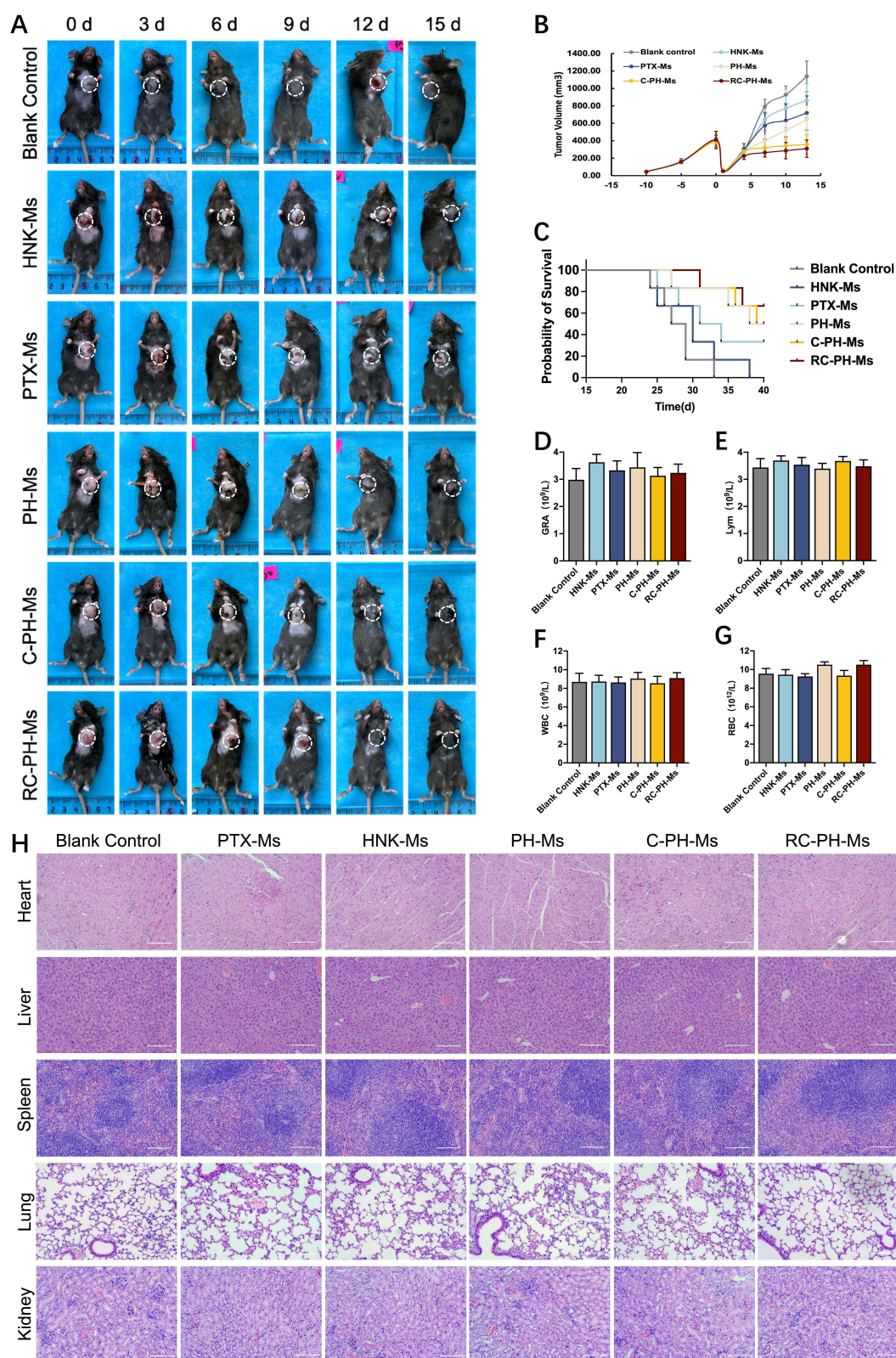
Figure 9 The effect of micelles on tumor recurrence and safety evaluation. (**A**) Recurrence of tumors in mice following surgical removal and subsequent treatment. Circles indicating tumor sites. (**B**) Variations in mouse tumor volume during the treatment process. (**C**) Survival rate curve for recurrence mice. (**D**–**G**) The counts of GRA (**D**), Lym (**E**), WBC (**F**) and RBC (**G**) in the whole blood of mice. (**H**) Representative images of HE staining in mouse organs. Scale bar, 50 μm. Data were presented as mean ± SD (n = 6).

([Figure 9B](#)). Furthermore, following micellar treatment, the survival duration of postoperative mice was extended to varying degrees ([Figure 9C](#)). Overall, RC-PH-Ms exhibited the most pronounced inhibitory effect on tumor recurrence and contributed to an increased survival rate among tumor-bearing mice, providing valuable insights for the prevention of ovarian cancer recurrence post-surgery.

Safety Evaluation of Preparation

Histopathological analysis of the major organs of mice was conducted to assess the in vivo toxicity of RC-PH-Ms, with results presented in [Figure 9H](#). HE staining images following the injection of RC-PH-Ms demonstrated that the major organs preserved normal cell morphology and no pathological abnormalities, such as tissue damage or inflammation were observed. These findings suggested that RC-PH-Ms did not exhibit significant toxic effects at the tissue level in mice. Moreover, all hematological indicators (GRA, LyM, WBC, RBC) were within the normal reference range when compared to the control group ([Figure 9D-G](#)). In summary, no significant toxic reactions were noted in the experimental group, indicating that the nanoparticles were both safe and reliable, with no apparent toxicity.

Conclusion

In this study, we proposed a novel ROS switch-type targeted drug delivery system designed to address the challenges of ovarian cancer proliferation, invasion, metastasis and recurrence. This RC-PH-Ms system featured an optimal particle size and was surface-modified with a ROS-responsive switch, allowing for the active targeting of micelles to the tumor microenvironment characterized by high ROS expression, subsequently exposing them to C-PH-Ms. The incorporation of a membrane-penetrating peptide enhanced the micellar dual targeting capabilities, facilitating the transport and localized release of therapeutic agents. Upon reaching the tumor site, the drug was released to inhibit tumor invasion, metastasis, angiogenesis and immune infiltration, thereby achieving an optimal therapeutic effect. This targeted drug delivery system demonstrated significant efficacy in combating tumors and preventing recurrence, highlighting its considerable potential for clinical applications in the treatment of ovarian cancer and other malignant tumors.

Data Sharing Statement

Data will be made available on request.

Acknowledgments

Author Contributions

All authors made a significant contribution to the work reported, whether that is in the conception, study design, execution, acquisition of data, analysis and interpretation, or in all these areas; took part in drafting, revising or critically reviewing the article; gave final approval of the version to be published; have agreed on the journal to which the article has been submitted; and agree to be accountable for all aspects of the work.

Disclosure

All authors declare that there are no conflicts of interest.

References

1. Cabasag CJ, Fagan PJ, Ferlay J, et al. Ovarian cancer today and tomorrow: a global assessment by world region and human development index using GLOBOCAN 2020. *Int J Cancer*. 2022;151(9):1535–1541. doi:10.1002/ijc.34002

2. Armstrong DK, Alvarez RD, Backes FJ, et al. NCCN guidelines(R) insights: ovarian cancer, version 3.2022. *J Natl Compr Canc Netw*. 2022;20 (9):972–980. doi:10.6004/jnccn.2022.0047

3. Nic Giolla Chomhaill C, Ward J, Dowling M. Fear of recurrence in women with ovarian cancer: a qualitative evidence synthesis. *Eur J Oncol Nurs*. 2024;68:102487. doi:10.1016/j.ejon.2023.102487

4. Shimizu A, Lengyel E. Decoding evolutionary trajectories of ovarian cancer metastasis. *Cancer Cell*. 2023;41(6):1008–1010. doi:10.1016/j. ccell.2023.05.011

5. Bayraktar E, Chen S, Corvigno S, Liu J, Sood AK. Ovarian cancer metastasis: looking beyond the surface. *Cancer Cell*. 2024;42(10):1631–1636. doi:10.1016/j.ccell.2024.08.016

6. Mei S, Chen X, Wang K, Chen Y. Tumor microenvironment in ovarian cancer peritoneal metastasis. *Cancer Cell Int*. 2023;23(1):11. doi:10.1186/ s12935-023-02854-5

7. Nomani A, Li G, Yousefi S, et al. Gadolinium-labeled affibody-XTEN recombinant vector for detection of HER2+ lesions of ovarian cancer lung metastasis using quantitative MRI. *J Control Release*. 2021;337:132–143. doi:10.1016/j.jconrel.2021.07.022

8. Ataseven B, du Bois A, Harter P, et al. Impact of abdominal wall metastases on prognosis in epithelial ovarian cancer. *Int J Gynecol Cancer*. 2016;26(9):1594–1600. doi:10.1097/IGC.0000000000000826

9. Guo J, Zou Y, Huang L. Nano delivery of chemotherapeutic ICD inducers for tumor immunotherapy. *Small Methods*. 2023;7(5):e2201307. doi:10.1002/smtd.202201307

10. Schoutrop E, Moyano-Galceran L, Lheureux S, et al. Molecular, cellular and systemic aspects of epithelial ovarian cancer and its tumor microenvironment. *Semin Cancer Biol*. 2022;86(Pt 3):207–223. doi:10.1016/j.semcancer.2022.03.027

11. Chen J, Yang L, Ma Y, Zhang Y. Recent advances in understanding the immune microenvironment in ovarian cancer. *Front Immunol*. 2024;15:1412328. doi:10.3389/fimmu.2024.1412328

12. Chiang Y, Lu LF, Tsai CL, et al. C-C chemokine receptor 4 (CCR4)-positive regulatory T cells interact with tumor-associated macrophages to facilitate metastatic potential after radiation. *Eur J Cancer*. 2024;198:113521. doi:10.1016/j.ejca.2023.113521

13. Luan X, Lei T, Fang J, et al. Blockade of C5a receptor unleashes tumor-associated macrophage antitumor response and enhances CXCL9-dependent CD8(+) T cell activity. *Mol Ther*. 2024;32(2):469–489. doi:10.1016/j.ymthe.2023.12.010

14. Kaur P, Singh SK, Mishra MK, Singh S, Singh R. Nanotechnology for boosting ovarian cancer immunotherapy. *J Ovarian Res*. 2024;17(1):202. doi:10.1186/s13048-024-01507-z

15. Liu H, Jiang S, Li M, et al. Dual enzyme-driven cascade reactions modulate immunosuppressive tumor microenvironment for catalytic therapy and immune activation. *ACS Nano*. 2024. doi:10.1021/acsnano.4c07374

16. Huang H, Li N, Wei X, et al. Biomimetic "Gemini nanoimmunoregulators" orchestrated for boosted photoimmunotherapy by spatiotemporally modulating PD-L1 and tumor-associated macrophages. *Acta Pharm Sin B*. 2024;14(3):1345–1361. doi:10.1016/j.apsb.2023.11.005

17. Ghisoni E, Morotti M, Sarivalasis A, et al. Immunotherapy for ovarian cancer: towards a tailored immunophenotype-based approach. *Nat Rev Clin Oncol*. 2024;21(11):801–817. doi:10.1038/s41571-024-00937-4

18. Chen Z, Yang S, Zhao Z, et al. Smart tumor cell-derived DNA nano-tree assembly for on-demand macrophages reprogramming. *Adv Sci*. 2024;11 (10):e2307188. doi:10.1002/advs.202307188

19. Ge F, Li Z, Hu J, Pu Y, Zhao F, Kong L. METTL3/m(6)A/IFIT2 regulates proliferation, invasion and immunity in esophageal squamous cell carcinoma. *Front Pharmacol*. 2022;13:1002565. doi:10.3389/fphar.2022.1002565

20. Nurullah M, Usmani Z, Ahmad S, Panda BP, Amin S, Mir SR. Purification and characterization of Taxol and 10-Deacetyl baccatin III from the bark, needles, and endophytes of Taxus baccata by preparative high-performance liquid chromatography, ultra-high-performance liquid chromatography-mass spectrometry, and nuclear magnetic resonance. *J Sep Sci*. 2023;46(6):e2200841. doi:10.1002/jssc.202200841

21. Mosca L, Ilari A, Fazi F, Assaraf YG, Colotti G. Taxanes in cancer treatment: activity, chemoresistance and its overcoming. *Drug Resist Updat*. 2021;54:100742. doi:10.1016/j.drup.2020.100742

22. Cao X, Chen J, Li B, et al. Promoting antibody-dependent cellular phagocytosis for effective macrophage-based cancer immunotherapy. *Sci Adv*. 2022;8(11):eabl9171. doi:10.1126/sciadv.abl9171

23. Fardous J, Omoso Y, Joshi A, et al. Development and characterization of gel-in-water nanoemulsion as a novel drug delivery system. *Mater Sci Eng C Mater Biol Appl*. 2021;124:112076. doi:10.1016/j.msec.2021.112076

24. Utreja P, Jain S, Tiwary AK. Evaluation of biosafety and intracellular uptake of Cremophor EL free paclitaxel elastic liposomal formulation. *Drug Deliv*. 2012;19(1):11–20. doi:10.3109/10717544.2011.621990

25. Liu WB, Wang HL, Chen L, et al. Cucurbitacin E inhibits cellular proliferation and induces apoptosis in melanoma by suppressing HSDL2 expression. *Chin Med*. 2022;17(1):28. doi:10.1186/s13020-022-00582-y

26. Banik K, Ranaware AM, Deshpande V, et al. Honokiol for cancer therapeutics: a traditional medicine that can modulate multiple oncogenic targets. *Pharmacol Res*. 2019;144:192–209. doi:10.1016/j.phrs.2019.04.004

27. Prasher P, Fatima R, Sharma M, et al. Honokiol and its analogues as anticancer compounds: current mechanistic insights and structure-activity relationship. *Chem Biol Interact*. 2023;386:110747. doi:10.1016/j.cbi.2023.110747

28. Ji H, Wang W, Li X, et al. Natural small molecules enabled efficient immunotherapy through supramolecular self-assembly in P53-mutated colorectal cancer. *ACS Appl Mater Interfaces*. 2022;14(2):2464–2477. doi:10.1021/acsami.1c16737

29. Fan W, Xiang J, Wei Q, et al. Role of micelle size in cell transcytosis-based tumor extravasation, infiltration, and treatment efficacy. *Nano Lett*. 2023;23(9):3904–3912. doi:10.1021/acs.nanolett.3c00449

30. Lu L, Chen H, Hao D, Zhang X, Wang F. The functions and applications of A7R in anti-angiogenic therapy, imaging and drug delivery systems. *Asian J Pharm Sci*. 2019;14(6):595–608. doi:10.1016/j.ajps.2019.04.004

31. Zhang Q, Yang Z, Zhang J, et al. Transmembrane modification of tumor vascular targeting peptide A7R as molecular cargo delivery tool. *Bioorg Chem*. 2024;145:107240. doi:10.1016/j.bioorg.2024.107240

32. Li FR, Yu Y, Du YM, et al. Borneol-modified schisandrin B micelles cross the blood-brain barrier to treat alzheimer's disease in aged mice. *ACS Chem Neurosci*. 2024;15(3):593–607. doi:10.1021/acschemneuro.3c00625

33. Pineiro L, Novo M, Al-Soufi W. Fluorescence emission of pyrene in surfactant solutions. *Adv Colloid Interface Sci*. 2015;215:1–12. doi:10.1016/j.cis.2014.10.010

34. Spleis H, Sandmeier M, Claus V, Bernkop-Schnurch A. Surface design of nanocarriers: key to more efficient oral drug delivery systems. *Adv Colloid Interface Sci*. 2023;313:102848. doi:10.1016/j.cis.2023.102848

35. Chen Y, Yang C, Mao J, Li H, Ding J, Zhou W. Spermine modified polymeric micelles with pH-sensitive drug release for targeted and enhanced antitumor therapy. *RSC Adv*. 2019;9(20):11026–11037. doi:10.1039/c9ra00834a

36. Ianevski A, Giri AK, Aittokallio T. SynergyFinder 3.0: an interactive analysis and consensus interpretation of multi-drug synergies across multiple samples. *Nucleic Acids Res*. 2022;50(W1):W739–W743. doi:10.1093/nar/gkac382

37. Larsson P, Pettersson D, Olsson M, et al. Repurposing proteasome inhibitors for improved treatment of triple-negative breast cancer. *Cell Death Discov*. 2024;10(1):57. doi:10.1038/s41420-024-01819-5

38. Ianevski A, Giri AK, Aittokallio T. SynergyFinder 2.0: visual analytics of multi-drug combination synergies. *Nucleic Acids Res*. 2020;48(W1):W488–W493. doi:10.1093/nar/gkaa216

39. Zheng S, Wang W, Aldahdooh J, et al. SynergyFinder plus: toward better interpretation and annotation of drug combination screening datasets. *Genomics Proteomics Bioinf*. 2022;20(3):587–596. doi:10.1016/j.gpb.2022.01.004

40. Chen C, Chen B, Lin Y, et al. Cardamonin attenuates iron overload-induced osteoblast oxidative stress through the HIF-1alpha/ROS pathway. *Int Immunopharmacol*. 2024;142(Pt A):112893. doi:10.1016/j.intimp.2024.112893

41. Nagaraj B, Sivasubramanian A, Musthafa SA, et al. Clerodane diterpene 3-deoxycaryoptinol (Clerodin) selectively induces apoptosis in human monocytic leukemia (THP-1) cells and upregulates apoptotic protein caspase-3. *Free Radic Biol Med*. 2024;225:925–932. doi:10.1016/j.freeradbiomed.2024.10.275

42. Zhang G, Gao Z, Guo X, et al. CAP2 promotes gastric cancer metastasis by mediating the interaction between tumor cells and tumor-associated macrophages. *J Clin Invest*. 2023;133(21). doi:10.1172/JCI166224

43. Wu C, Zheng C, Chen S, et al. FOXQ1 promotes pancreatic cancer cell proliferation, tumor stemness, invasion and metastasis through regulation of LDHA-mediated aerobic glycolysis. *Cell Death Dis*. 2023;14(10):699. doi:10.1038/s41419-023-06207-y

44. Whiteley AE, Ma D, Wang L, et al. Breast cancer exploits neural signaling pathways for bone-to-meninges metastasis. *Science*. 2024;384(6702):eadh5548. doi:10.1126/science.adh5548

45. Carrera-Aguado I, Marcos-Zazo L, Carrancio-Salan P, Guerra-Paes E, Sanchez-Juanes F, Munoz-Felix JM. The inhibition of vessel co-option as an emerging strategy for cancer therapy. *Int J mol Sci*. 2024;25(2):921. doi:10.3390/ijms25020921

46. Wei X, Chen Y, Jiang X, et al. Mechanisms of vasculogenic mimicry in hypoxic tumor microenvironments. *mol Cancer*. 2021;20(1):7. doi:10.1186/s12943-020-01288-1

47. Cannell IG, Sawicka K, Pearsall I, et al. FOXC2 promotes vasculogenic mimicry and resistance to anti-angiogenic therapy. *Cell Rep*. 2023;42(8):112791. doi:10.1016/j.celrep.2023.112791

48. Liu Y, Hu Q, Dong W, Liu S, Zhang H, Gu Y. Alginate/gelatin-based hydrogel with soy protein/peptide powder for 3D printing tissue-engineering scaffolds to promote angiogenesis. *Macromol Biosci*. 2022;22(4):e2100413. doi:10.1002/mabi.202100413

49. Kusaczuk M, Tovar-Ambel E, Martin-Cabrera P, et al. Cytotoxicity, proapoptotic activity and drug-like potential of quercetin and kaempferol in glioblastoma cells: preclinical insights. *Int J mol Sci*. 2024;25(19):10740. doi:10.3390/ijms251910740

50. Hu H, Ma T, Liu N, et al. Immunotherapy checkpoints in ovarian cancer vasculogenic mimicry: tumor immune microenvironments, and drugs. *Int Immunopharmacol*. 2022;111:109116. doi:10.1016/j.intimp.2022.109116

51. Gunassekaran GR, Poongkavithai Vadevoo SM, Baek MC, Lee B. M1 macrophage exosomes engineered to foster M1 polarization and target the IL-4 receptor inhibit tumor growth by reprogramming tumor-associated macrophages into M1-like macrophages. *Biomaterials*. 2021;278:121137. doi:10.1016/j.biomaterials.2021.121137

52. Gao J, Liang Y, Wang L. Shaping polarization of tumor-associated macrophages in cancer immunotherapy. *Front Immunol*. 2022;13:888713. doi:10.3389/fimmu.2022.888713

53. Boutilier AJ, Elsawa SF. Macrophage polarization states in the tumor microenvironment. *Int J mol Sci*. 2021;22(13):6995. doi:10.3390/ijms22136995

54. Konstantinopoulos PA, Matulonis UA. Clinical and translational advances in ovarian cancer therapy. *Nat Cancer*. 2023;4(9):1239–1257. doi:10.1038/s43018-023-00617-9